

An enhanced multi-scale approach for masonry wall computations with localization of damage

T. J. Massart^{1,*},[†], R. H. J. Peerlings^{2,‡} and M. G. D. Geers^{2,§}

¹*Structural and Material Computational Mechanics Department CP 194/5, Université Libre de Bruxelles, Av. F.-D. Roosevelt 50, 1050 Brussels, Belgium*

²*Department of Mechanical Engineering, Eindhoven University of Technology, P.O. Box 513, 5600 MB Eindhoven, The Netherlands*

SUMMARY

This contribution presents a multi-scale framework for the computational study of masonry structures. In order to overcome the need for excessively complex closed-form constitutive equations, a first-order computational homogenization framework is applied to infer the non-linear material behaviour of brick masonry in the presence of quasi-brittle damage. A localization analysis is carried out based on the macroscopic homogenized tangent stiffness. It is shown that localization is detected along preferential orientations, which are consistent with the underlying mesostructural failure patterns and with the applied loading. The macroscopic description is enhanced with a finite width damage band model in order to allow the treatment of macroscopic localization resulting from damage growth in the constituents. As a result of the use of homogenization techniques on finite volumes and the presence of quasi-brittle constituents, mesostructural snap-back may occur in the homogenized material response. A methodology to introduce this type of response in the multi-scale technique is proposed. The numerical implementation of the multi-scale solution scheme using a finite element method is outlined. The results obtained by the framework are illustrated by means of elementary examples, and by an example of a structural wall computation. Copyright © 2006 John Wiley & Sons, Ltd.

Received 23 May 2004; Revised 3 May 2006; Accepted 18 May 2006

KEY WORDS: multi-scale modelling; masonry; computational homogenization; damage-induced anisotropy; localization; embedded discontinuities; snap-back; structural computations

*Correspondence to: T. J. Massart, Structural and Material Computational Mechanics Department CP 194/5, Université Libre de Bruxelles, Av. F.-D. Roosevelt 50, 1050 Brussels, Belgium.

[†]E-mail: thmassar@smc.ulb.ac.be

[‡]E-mail: R.H.J.Peerlings@tue.nl

[§]E-mail: M.G.D.Geers@tue.nl

Contract/grant sponsor: Région Wallonne, Belgium; contract/grant number: 215089 (HOMERE)

1. INTRODUCTION

Due to the complexity and the heterogeneous nature of the material used, the design of masonry structures is essentially based on codes and rules of thumb, often leading to a lack of control on safety factors and over-dimensioning. The commonly made conservative approximations in design are too inaccurate in order to assess the residual strength and load-bearing capacity of such structures. In this respect, modern computational methods start to emerge as valuable tools for the study of masonry structures [1, 2]. The interest in such modelling tools originates from their rational approach towards stability analyses, allowing to complement codes, rules of thumb and engineering experience. However, these computational approaches require reliable constitutive models which are generally difficult to formulate for degrading masonry.

Masonry may be considered as a two-phase composite material in which the phases, bricks and mortar, are assembled in a periodic manner. This periodic mesostructure and the different elastic characteristics of the two phases render the elastic behaviour of masonry anisotropic. In addition, the mortar phase is relatively weak, which due to the periodic arrangement of the phases leads to a stiffness degradation along preferential orientations. This results in a pronounced crack-induced anisotropy which may have a strong impact on stress redistributions [3]. The initial as well as the induced anisotropy of the overall material are strongly coupled to the underlying mesostructure, particularly to the geometry, the stacking mode, and the material properties of the brick and mortar. The mesostructure therefore has an important effect on the structural failure mechanisms that are observed. This suggests that the mesostructure should be taken into account in accurate structural failure analyses.

The formulation of models which represent this type of behaviour is rather delicate. Dedicated models were developed, which can be classified according to their objectives and their scales of representation. A first class makes use of a mesoscopic approach in which the constituents are modelled individually [4, 5]. Potential crack sites are represented by interfaces, in which all material non-linearity is concentrated. This approach allows to accurately capture most of the in-plane failure mechanisms, but it is inefficient for large-scale structural computations because of the excessive computational effort required.

A second class of models successfully overcomes this drawback by formulating closed-form macroscopic constitutive laws for an equivalent homogeneous continuum, which link average stresses to average strains in a phenomenological manner [6–8]. However, overall closed-form laws are difficult to formulate, in particular when the interaction between the initial and damage-induced anisotropy has to be represented [9]. Furthermore, their experimental identification and quantification is usually difficult and expensive.

The drawbacks of the approaches described above may be alleviated by a multi-scale approach, where the mesoscopic and macroscopic scales of representation are intrinsically coupled. A first class of multi-scale approaches bridges both scales by the identification of macroscopically used material parameters from mesoscopic models, which solves at least partially the identification problem in closed-form macroscopic descriptions. The actual structural computation is then performed with the macroscopic model only. Closed-form constitutive relations still need to be postulated for both scales in such an approach. This strategy was used for the elastic behaviour of masonry [10, 11], with extensions to the non-linear regime in References [12, 13] for specific loading cases.

In spite of their efficiency, formulating and identifying accurate closed-form macroscopic constitutive laws still constitutes a major difficulty in the above approach. This may be overcome by adopting a multi-scale approach, in which both scales of representation are fully coupled in the

entire structural computation. The overall material behaviour is determined 'on-line' during the structural computation by computational homogenization, i.e. by 'interrogating' a representative volume element (RVE) of the material. This idea has been used to model the plastic behaviour of heterogeneous polymer and metal systems [14–16]. Such an approach was developed for masonry in this spirit in Reference [17], but with an elastic-brittle representation for the constituents. This approach allows to capture complex overall effects such as damage-induced anisotropy on the basis of simple isotropic constitutive relations postulated at the level of the constituents, thereby avoiding complex macroscopic closed-form formulations. Material data can be directly implemented at the scale of individual components, and the identification problem is thus transferred to the mesoscopic level, where reliable experimental data are more readily available [18]. Evidently, the main disadvantage of this type of approach resides in the increased computational cost, but it is believed that this cost may become acceptable as a result of the steady growth of the available computing power.

The degradation process which we aim to model is accompanied by localization of damage in narrow zones, which ultimately leads to failure [19]. In a multi-scale context, this may happen for the description at both the structural and the constituent scales. Softening in the material response in a local continuum generally leads to ill-posed boundary value problems, an undetermined width of the localization zones, and a non-objective energy dissipation [19]. The treatment of localization of damage at the scale of the constituents can be handled correctly with appropriate (non-local) techniques since closed-form constitutive laws are used for this purpose. At the macroscopic scale, the adopted multi-scale approach [14, 20] homogenizes the mesoscopic description towards a classical stress–strain response, which naturally complies with the principle of local action. The occurrence of localization at the macroscopic scale will therefore be taken into account here by the introduction of an embedded localization band, the width of which is determined from the periodicity of the mesostructure.

Due to the softening of the masonry constituents, mesoscopic localization eventually appears. Depending on the relative volumes of the phases, the mesostructural homogenized response may show snap-back due to the inability of the damaging part of the mesostructure (e.g. the mortar joints) to completely dissipate the energy which is released in the unloading parts (usually the bricks). From a macroscopic viewpoint, this behaviour can be regarded as a 'constitutive snap-back', although it actually appears as a mesostructural effect that ensues from the averaged behaviour of a finite volume. Standard strain-driven nested solution schemes cannot deal with this mesostructural snap-back and an extension is therefore needed as this phenomenon is expected to occur in realistic computations.

This contribution presents a new localization-enhanced multi-scale solution procedure which deals with the difficulties of conventional computational homogenization as outlined above. It allows to handle damage localization at different scales in a physically motivated manner and to include non-orthotropic anisotropy effects naturally in structural scale computations, two features hardly met in existing masonry models. It is based on the following salient new features: (i) the coupling of macroscopic localization detection with a homogenization procedure leading to a physically based description of damage preferential orientations, (ii) the definition of an embedded band model allowing to incorporate a motivated energy dissipation in the localization behaviour at the macroscopic scale, (iii) the improvements of scale transitions allowing to treat fine-scale snap-back effects together with a branching technique for the localized response.

The paper is structured as follows. The principles of the adopted multi-scale framework are first recalled in Section 2, after which they are refined for the modelling of masonry. The principles

used to detect macroscopic localization by means of embedded bands are highlighted in Section 3, which also illustrates for two typical loading cases that mesostructurally motivated average cracking orientations can be detected based on a localization analysis performed on a masonry unit cell. The governing equations of a first-order multi-scale scheme are modified, taking into account localization by means of finite-sized embedded bands, as highlighted in Section 4. The scale transition improvements based on mesostructural dissipation control are introduced in Section 5 in order to trace mesostructural snap-back paths in the homogenized material responses. Section 6 details the implementation of the model by means of the finite element method, including the branch switching procedure for the introduction of localization bands. The proposed framework is applied to some elementary tests and to a structural application in Section 7. Finally, conclusions on the added value and innovative character of the proposed framework, as well as necessary future developments, are given in Section 8.

2. LOCAL MULTI-SCALE SOLUTION SCHEME

2.1. Principles and assumptions

The multi-scale computational scheme presented in Reference [21] extracts the macroscopic material behaviour from a RVE of the material. For the application to masonry structures, the coarse or macroscopic scale is the structural scale. The fine or mesoscopic scale is that of individual bricks and joints. With the exception of the displacement field, uppercase symbols denote macroscopic quantities throughout this paper, while lowercase symbols represent mesoscopic variables. The gradient operator ∇ and the tangent stiffness operator ${}^4\mathbf{L}$ are suffixed by a lowercase m for mesoscopic quantities, and by an uppercase M for macroscopic quantities.

The key principle of the nested multi-scale approach is summarized in Figure 1. A macroscopic strain \mathbf{E} is obtained at each iteration of the non-linear macroscopic solution procedure for all macroscopic sampling points (Gauss points). The solution procedure then requires the corresponding macroscopic stress tensor Σ . Instead of feeding \mathbf{E} into a closed-form constitutive relation at the macro-scale, it is transferred to the meso-scale by applying it in an average sense to a RVE (macro-meso scale transition). This allows to define a boundary value problem (BVP) at the

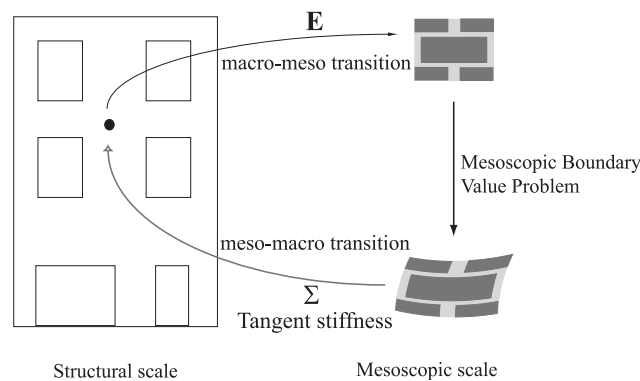


Figure 1. Principle of first-order multi-scale solution scheme.

meso-scale. The response of the RVE is obtained as the solution of this boundary value problem. As a result, the mesoscopic strain field $\boldsymbol{\varepsilon}$, the mesoscopic stress field $\boldsymbol{\sigma}$, and potentially other field variables inside the RVE are available. The macroscopic stress $\boldsymbol{\Sigma}$ is then computed by averaging the mesoscopic stress field (meso–macro transition). The macroscopic stress–strain response of the material is thus fully determined, although it is only available numerically and not in terms of macroscopic constitutive relations. The meso–macro transition also furnishes the constitutive tangent, which relates variations of $\boldsymbol{\Sigma}$ to variations of \boldsymbol{E} , for the next iteration of the macroscopic solution procedure [20].

The scale transition procedure attributes a stress–strain response extracted from a mesoscopic *structure* to a macroscopic *material point*. The validity of the approach is therefore theoretically restricted to situations in which the principle of separation of scales applies, i.e. in which the mesoscopic characteristic length is much smaller than the length scale associated to variations of the macroscopic fields [16].

2.2. Scale transitions and mesoscopic boundary value problem

The macro–meso scale transition consists in applying the macroscopic strain to a RVE in an average sense. Boundary conditions are therefore required, which are defined such that the volume average of the mesoscopic strain on the RVE equals the imposed macroscopic strain. Periodic boundary conditions are found to deliver the best results in terms of the stiffness estimation for random mesostructures [22]. The periodicity of the initial mesostructure of masonry further suggests the use of this periodicity requirement. The displacement field (in each point of the mesostructure) is characterized by

$$\boldsymbol{u} = \boldsymbol{E}\boldsymbol{x} + \boldsymbol{w} \quad (1)$$

where \boldsymbol{E} is the macroscopic strain tensor, \boldsymbol{x} is the position vector within the RVE, and \boldsymbol{w} is a mesoscopic displacement fluctuation field originating from the heterogeneity of the material. The volume average of the mesoscopic strain field $\boldsymbol{\varepsilon}$ ensuing from relation (1) is given by

$$\langle \boldsymbol{\varepsilon} \rangle = \frac{1}{V_{\text{RVE}}} \int_{V_{\text{RVE}}} [\nabla_m(\boldsymbol{E}\boldsymbol{x} + \boldsymbol{w})]^{\text{sym}} dV = \boldsymbol{E} + \frac{1}{V_{\text{RVE}}} \int_{\partial V_{\text{RVE}}} (\boldsymbol{w}\boldsymbol{n})^{\text{sym}} dS \quad (2)$$

If the fluctuation field \boldsymbol{w} is assumed to be periodic, the boundary integral in (2) vanishes, and hence $\langle \boldsymbol{\varepsilon} \rangle = \boldsymbol{E}$. Practically, the periodicity of \boldsymbol{w} at the boundary is imposed by means of linear tying relations. The macroscopic strain is imposed through the displacements of three controlling points, see Section 2.3.

In addition to the kinematic constraint defining the macro–meso scale transition, homogenization schemes usually rely on a work equivalence to identify the macroscopic stress tensor. This equivalence between the variations of macroscopic and mesoscopic work is known as the Hill–Mandel condition and reads as

$$\boldsymbol{\Sigma} : \delta\boldsymbol{E} = \frac{1}{V_{\text{RVE}}} \int_{V_{\text{RVE}}} \boldsymbol{\sigma} : \delta\boldsymbol{\varepsilon} dV_{\text{RVE}} \quad \forall \delta\boldsymbol{\varepsilon} \quad (3)$$

where $\delta \mathbf{E}$ and $\delta \boldsymbol{\varepsilon}$ are related as defined above. Using mesoscopic equilibrium and the Gauss theorem, the displacement field (1) may be introduced in (3), yielding

$$\boldsymbol{\Sigma} : \delta \mathbf{E} = \frac{1}{V_{RVE}} \left(\int_{\partial V_{RVE}} (\mathbf{p}\mathbf{x})^{sym} dS_{RVE} \right) : \delta \mathbf{E} + \frac{1}{V_{RVE}} \left(\int_{\partial V_{RVE}} (\mathbf{p} \cdot \mathbf{w})^{sym} dS_{RVE} \right) \quad (4)$$

where \mathbf{p} is the traction vector acting on the boundary S_{RVE} of the RVE. Taking into account the periodicity of \mathbf{w} and the resulting anti-periodicity of \mathbf{p} at the boundary, the macroscopic stress tensor is obtained as

$$\boldsymbol{\Sigma} = \frac{1}{V_{RVE}} \int_{\partial V_{RVE}} (\mathbf{p}\mathbf{x})^{sym} dS_{RVE} \quad (5)$$

in terms of mesoscopic quantities at the RVE boundary.

2.3. Choice of the mesoscopic representative volume element

The selection of the RVE should be performed with care, in order to limit the computational effort at the mesoscopic level, still capturing all possible failure mechanisms. Different RVE shapes and sizes have been used in the literature for masonry [10, 13, 17]. Note that any periodic RVE delivers the same results as long as the average behaviour remains unique, i.e. before localization in an infinitesimal strain setting. Based on the periodicity of the initial mesostructure of masonry, the RVE is therefore chosen as the smallest possible periodic unit cell of the mesostructure. This choice is based on the assumption that the average stiffness degradation is mainly due to the arrangement of constituents and will be correctly captured—including damage-induced anisotropy effects—using such a cell. The unit cell used here is illustrated for the case of running bond masonry in Figure 2 and consists of a brick surrounded by half a joint. The running bond periodicity conditions have been indicated on the cell by arrows linking mutually tied boundary segments. It is noted that the use of this periodic cell throughout the entire degradation process typically describes failure mechanisms which satisfy the periodicity conditions illustrated in Figure 3(a), since periodicity implies that the damage pattern in a unit cell attributed to a macroscopic material point repeats itself in the vicinity of this point. Actual damaged configurations usually exhibit strongly localized crack patterns at the macroscopic scale as depicted in Figure 3(b). A methodology to represent macroscopically localized states will therefore be developed in the next sections. The proposed unit cell was already used in References [3, 23], together with an isotropic damage model at the mesoscopic scale. It was shown to deliver realistic average responses for non-perforated bricks, both in terms of load-bearing capacity and observed failure modes, including non-orthotropic damaging effects.

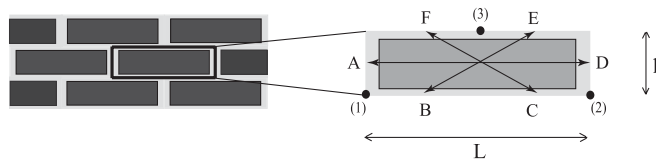


Figure 2. Unit cell and periodicity tyings for running bond masonry.

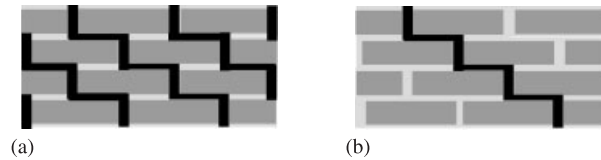


Figure 3. Influence of the periodicity assumption on the representation of failure patterns in the vicinity of a macroscopic material point: (a) failure pattern satisfying the periodicity condition; and (b) real failure pattern.

The three macroscopic strain components are imposed on the cell through imposed displacements of three controlling points, indicated in Figure 2 by (1), (2) and (3). These displacements may be expressed in terms of the components of the macroscopic infinitesimal strain tensor as

$$\begin{aligned}(u_1, v_1) &= (0, 0) \\ (u_2, v_2) &= (LE_{XX}, 0) \\ (u_3, v_3) &= (2hE_{XY} + \frac{1}{2}E_{XX}, hE_{YY})\end{aligned}\quad (6)$$

where L and h are the horizontal and vertical size of the unit cell, respectively. The periodicity of the fluctuation field is then imposed through the relations

$$\begin{aligned}\mathbf{u}(\mathbf{x}_D) &= \mathbf{u}(\mathbf{x}_A) + \mathbf{u}_2 - \mathbf{u}_1 \\ \mathbf{u}(\mathbf{x}_E) &= \mathbf{u}(\mathbf{x}_B) + \mathbf{u}_3 - \mathbf{u}_1 \\ \mathbf{u}(\mathbf{x}_F) &= \mathbf{u}(\mathbf{x}_C) + \mathbf{u}_3 - \mathbf{u}_2\end{aligned}\quad (7)$$

where $\mathbf{x}_A, \dots, \mathbf{x}_F$ are the position vectors of points on the boundary segments A, \dots, F .

Due to periodicity, the macroscopic stress can be obtained directly from the external forces $\mathbf{f}^{(i)}$ acting on three controlling points only [20]:

$$\boldsymbol{\Sigma} = \frac{1}{V_{\text{RVE}}} \sum_{i=1}^3 \mathbf{x}^{(i)} \mathbf{f}^{(i)} \quad (8)$$

where $\mathbf{x}^{(i)}$ is the position of point (i) . A macroscopic consistent tangent operator can be obtained by a static condensation of the mesostructural tangent stiffness matrix towards the controlling points [20]. This condensed tangent relation, applying to a mesoscopically converged state, may be written as

$$\sum_{p=1}^3 \mathbf{K}_M^{(np)} \cdot \delta \mathbf{u}^{(p)} = \delta \mathbf{f}^{(n)}, \quad n = 1, 2, 3 \quad (9)$$

where $\mathbf{K}_M^{(np)}$ is a second-order tensor relating the variations of the displacement vector of the controlling point (p) to the variations of the mesoscopic force vector at controlling point (n) .

Combining relations (1), (8) and (9) allows to define the constitutive tangent ${}^4\mathbf{L}_M$ according to

$$\delta\Sigma = \underbrace{\left(\sum_{n=1}^3 \sum_{p=1}^3 \mathbf{x}^{(n)} \mathbf{K}_M^{(np)} \mathbf{x}^{(p)} \right)^{(rs)}}_{{}^4\mathbf{L}_M} : \delta\mathbf{E} \tag{10}$$

where $(\cdot)^{(rs)}$ denotes condensation with right symmetrization to relate the symmetric Cauchy stresses to the symmetric infinitesimal strain tensor.

3. LOCALIZATION OF DAMAGE AT MESOSCOPIC AND MACROSCOPIC SCALES

An important issue in modelling failure by continuum methods is the localization of deformation and degradation. Classical constitutive theories notoriously suffer from pathological localization when used to model damage and fracture [19]. At a certain stage of the degradation process, further deformation tends to localize in a surface, while the remaining volume unloads elastically. As a consequence, no energy dissipation is predicted anymore. This deficiency is intimately linked to a loss of well-posedness of the underlying boundary value problem. In numerical analyses it results in an undesired sensitivity of the analysis results with respect to the spatial discretization. Damage localization thus calls for a specific treatment, in the present case at both the mesoscopic and macroscopic scales.

3.1. Mesoscopic scale localization—implicit gradient damage

A number of approaches have been proposed in order to enhance continuum formulations by including an intrinsic length parameter to avoid the ill-posedness [19, 24, 25]. For the present study, simple non-perforated bricks are assumed. As a result, an isotropic damage model is used at the mesoscopic scale, assuming that damage-induced anisotropy at the macroscopic scale essentially originates from the geometrical arrangement of the constituents. It is recognized that other mesoscopic models could be used in order to capture certain effects, such as an independent energy dissipation in mode I and mode II fracture, or dilatancy. However, the principles presented in the remainder of the paper will remain mostly independent of the modelling choice at the mesoscopic scale.

Pathological mesoscopic localization is prevented here by the use of a gradient damage model [24]. The internal length scale included in this model implicitly sets the width of damage bands and thus prohibits bands of zero width. A scalar, isotropic damage quantity is introduced for each constituent in the stress–strain relationship

$$\boldsymbol{\sigma} = (1 - D) {}^4\mathbf{L}_m : \boldsymbol{\varepsilon} \tag{11}$$

The damage value D is deduced from a damage evolution law based on the strain history through a parameter κ , which represents the most severe strain state experienced so far by the material

$$D = D(\kappa) \tag{12}$$

In order to determine whether a strain state change is accompanied by further damage growth, a damage loading function is expressed in terms of a non-local or averaged scalar measure of the

strain state $\bar{\varepsilon}_{\text{eq}}$ and of the parameter κ as

$$f(\bar{\varepsilon}_{\text{eq}}, \kappa) = \bar{\varepsilon}_{\text{eq}} - \kappa \quad (13)$$

The damage loading function f enters the Kuhn–Tucker relations

$$f \leq 0, \quad \dot{\kappa} \geq 0, \quad f \dot{\kappa} = 0 \quad (14)$$

and an initial condition is defined for κ

$$\kappa(t=0) = \kappa_i \quad (15)$$

The non-local $\bar{\varepsilon}_{\text{eq}}$ field is introduced as the solution of an averaging partial differential equation incorporating a material intrinsic length scale l_c in the meso-scale description:

$$\bar{\varepsilon}_{\text{eq}} - l_c^2 \nabla_m^2 \bar{\varepsilon}_{\text{eq}} = \varepsilon_{\text{eq}} \quad (16)$$

This partial differential equation is complemented by a boundary condition of the Neumann type applied at the interface between materials.

$$\nabla_m \bar{\varepsilon}_{\text{eq}} \cdot \mathbf{n} = 0 \quad (17)$$

Details related to the damage criteria used for the constituents and the application of this framework for masonry mesostructures are discussed in References [3, 23], where it is shown that realistic results are obtained.

3.2. Macroscopic scale localization detection

The macroscopic continuum used in the multi-scale approach remains *local*, and a pathologically localized response may therefore be expected at the macro-scale. The characteristic spatial variation of the macroscopic solution would localize in an infinitesimal volume, whereas that of the underlying mesostructural analysis remains finite, thus violating the scale separation which was assumed *a priori* between the meso- and macro-scale. For disordered random heterogeneous materials, an elegant solution to the above macroscopic localization issue was proposed in Reference [16], by extending the macroscopic continuum with a higher-order kinematic measure and a corresponding higher-order stress in the sense defined by Toupin and Mindlin [26, 27]. In this second-order framework, the physical size of the mesostructural RVE enters the macroscopic equilibrium problem, and provides the length scale on which the macroscopic deformation field tends to localize. The second-order description however requires a sufficiently fine discretization of the localized zone at the macroscopic scale to capture its kinematics. In the case of masonry, damage appears at the lowest scale, below the unit cell size. As a result, the use of a macroscopic gradient-enhanced description would not give any benefit in this case, as the required discretization would be of the same order as the mesoscopic discretization. In the case of masonry, macroscopic higher-order continua will be avoided here by further exploiting the periodicity of the mesostructure. For each possible failure mechanism, a localization bandwidth can be determined in a natural way by identifying the smallest possible period over which the damage pattern may be repeated. This is illustrated in Figure 4 for the case of a staircase crack pattern. For most of the crack patterns, this bandwidth can be deduced from the unit cell size perpendicular to the considered average crack orientation. The inclusion of such localization bands requires the following ingredients: (i) a criterion to decide when to introduce a localization band, (ii) a criterion to determine its orientation.

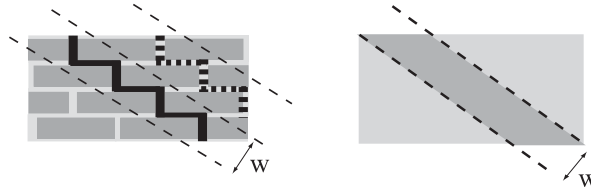


Figure 4. Extraction of a localization bandwidth based on the periodicity of the material. The dashed crack pattern indicates the periodicity for the considered pattern.

Retrieving these localization characteristics relies here on pointwise concepts as defined for closed-form constitutive relations. In homogeneous problems, the appearance of a band in which further growth of damage localizes may be considered as the bifurcation of a secondary solution from the homogeneous fundamental solution. This approach is used in classical continuum mechanics to derive the conditions for the onset of localization, see, e.g. Reference [28], and is related to the mathematical concepts of loss of ellipticity [19, 25]. For continuous bifurcation—i.e. with the same material tangent ${}^4\mathbf{L}_M$ at both sides of the discontinuity—macroscopic localization in an orientation \mathbf{n} potentially occurs whenever the condition

$$\det(\mathbf{A}) = \det(\mathbf{n} \cdot {}^4\mathbf{L}_M \cdot \mathbf{n}) = 0 \tag{18}$$

is fulfilled. Under the linear comparison solid assumption, meeting this criterion is a sufficient condition for the boundary value problem to become ill-posed. Note that this condition was later extended to discontinuous bifurcations—where the tangent ${}^4\mathbf{L}_M$ is no longer identical on both sides of the discontinuity—see Reference [29]. The set of orientations \mathbf{n} for which localization may appear is then determined by the inequality

$$\det(\mathbf{n} \cdot {}^4\mathbf{L}_M \cdot \mathbf{n}) \leq 0 \tag{19}$$

In a multi-scale setting, the loss of uniqueness in the underlying mesostructural problem may also be used to detect macroscopic localization. A necessary condition for this to occur is the loss of positive definiteness of the underlying mesostructural discretized stiffness [19]. Since the homogenized material stiffness is obtained from this quantity, this can be detected based on the eigenvalues of the homogenized stiffness $\lambda_i^{\mathbf{L}_M}$ with the condition

$$\lambda_{i,\min}^{\mathbf{L}_M} \leq 0 \tag{20}$$

which corresponds to a limit point in the homogenized stress–strain response.

3.3. Illustration of macroscopic localization analysis

In this section, the use of these localization conditions in the computational homogenization scheme for running bond masonry is illustrated. An analysis is performed on the eigenspectrum of the acoustic tensor associated with the macroscopic material tangent ${}^4\mathbf{L}_M$ obtained from Equation (10). An eigenvalue analysis of the homogenized tangent stiffness itself is also performed. These analyses are done for the entire deformation path in a uniformly and proportionally stressed ‘structure’. The macroscopic ‘structure’ consists of a single finite element which has the precise dimensions of a single unit cell in order to obtain the same load–displacement curves. The considered brick

has dimensions $L \times h \times e$ equal to $165 \times 52 \times 100 \text{ mm}^3$ with mortar joints that are 10 mm thick. The mesostructure is represented by means of a finite element mesh containing 396 eight-noded elements and 1440 nodes. A plane stress behaviour is assumed since the failure patterns for the considered loading cases are not strongly affected by three-dimensional effects [23]. The damage criteria used for the brick and mortar materials are the same as in Reference [23], namely a maximum principal stress criterion for the brick material and a Drucker–Prager-like criterion with a compressive cap for mortar. The material parameters used in this illustration are reported in Table I. The internal length parameter of the non-local damage model is denoted l_c , while f_t and f_c denote the uniaxial tensile and the uniaxial compressive strengths of the materials, respectively. The compressive cap used for the mortar criterion is controlled by the triaxial strength parameters f_b and f_h . Advanced path following techniques [30] are used to follow the solution path up to complete failure.

Two loading cases are investigated here, which both lead to typical failure patterns. Vertical compression is first combined with a small amount of horizontal tension, leading to a failure mechanism which involves mode I failure of the head joints and vertical cracking of the bricks. The second test considers a combination of vertical compression and shear and leads to the formation of a staircase crack. Figure 5 shows the final damage patterns that are typically obtained for the two loading cases. If complete failure is assumed, an overall crack direction can be identified for each of the patterns, based on geometric arguments only, as indicated by the normal vector \mathbf{n} in Figure 5. For the geometry used here, orientations of $\Theta = 0^\circ$ and $\Theta = 54.7^\circ$ are found, respectively, for the considered loading cases. These are the directions which one would like to retrieve from the analysis at the mesostructural level, without any prior knowledge of the final failure pattern.

3.3.1. Vertical compression combined with horizontal tension. The first loading case, along $(\Sigma_{xx}, \Sigma_{yy}, \Sigma_{xy}) = (0.5, -1, 0)$, leads to mode I failure of the head joints, followed by

Table I. Mesoscopic material parameters.

Material	E (MPa)	ν	l_c (mm)	f_t (MPa)	G_f (J/m ²)	f_c (MPa)	f_b (MPa)	f_h (MPa)
Brick	16 700	0.15	1.73	0.75	16.2	15	—	—
Mortar	3900	0.20	1.73	0.13	9	5.6	8.72	7.45

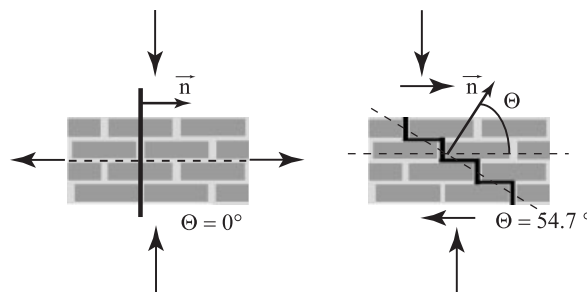


Figure 5. Average crack orientations defined by their normal \mathbf{n} for the considered failure patterns.

vertical cracking in the brick due to a combined tension-compression stress state. As proportional loading is applied, all stress components remain proportional to the imposed load factor. The load–displacement curve depicted on the left in Figure 6 represents the variation of the load factor as a function of the horizontal displacement of the right controlling node of the unit cell. The state corresponding to each point denoted by a capital letter in Figure 6 is analysed below. The evolution of the lowest eigenvalue of the homogenized tangent operator ${}^4\mathbf{L}_M$ is given in the right diagram of Figure 6 as a function of the same displacement. The damage distribution in the cell for each state is shown in Figure 7 together with the corresponding acoustic tensor eigenspectrum. The eigenspectrum for damaged configurations is normalized by dividing it by the homogenized horizontal stiffness of the undamaged material, $L_{1111} = 12\,957$ MPa. In state A, the failure of the head joints is accompanied by a decrease of the lowest eigenvalue, particularly for angles around $\Theta = 0^\circ$. The eigenvalue for $\Theta = 90^\circ$ is affected much less by the initial stages of damage growth. At the same time, the lowest eigenvalue of the homogenized tangent stiffness also decreases (Figure 6, right). A portion of the acoustic tensor eigenspectrum enters the negative range when damage is initiated in the brick, Figure 7, state B, indicating the possibility for localization according to the discontinuous bifurcation criterion (19). The negative portion of the eigenspectrum is centred around 0° . It exhibits at this stage a local maximum for $\Theta = 0^\circ$ and two local minima at approximately $\Theta = \pm 20^\circ$. These minima, which are identical in intensity, stem from the original curve as in state A, and disappear almost immediately after they have become negative. Simultaneously, the lowest eigenvalue of the homogenized tangent stiffness becomes negative, see Figure 6, point B. When the computation is continued on this fundamental path, the eigenvalue analysis indicates a vertical band ($\Theta = 0^\circ$), which clearly corresponds with the orientation predicted in Figure 5. Upon complete failure, the localization orientation still corresponds to a minimum in the acoustic tensor eigenspectrum (states C and D).

These results show that the localization analysis on the homogenized tangent material stiffness allows to detect the macroscopic bifurcation in terms of the applied load level and its orientation in a consistent way with the corresponding mesostructural damage pattern. Note in particular that

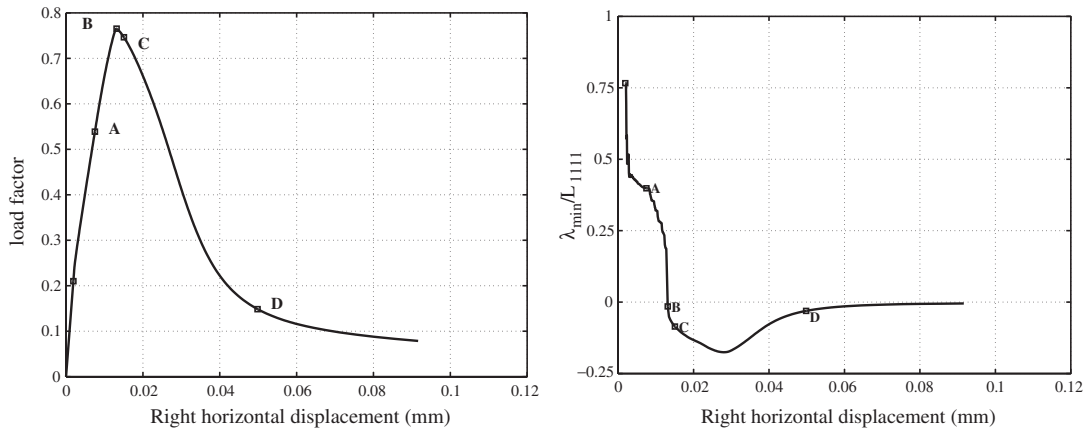


Figure 6. (left) Loading factor vs horizontal displacement of the right controlling node of the cell for vertical compression combined with horizontal tension, (right) Evolution of the lowest eigenvalue of the homogenized tangent operator.

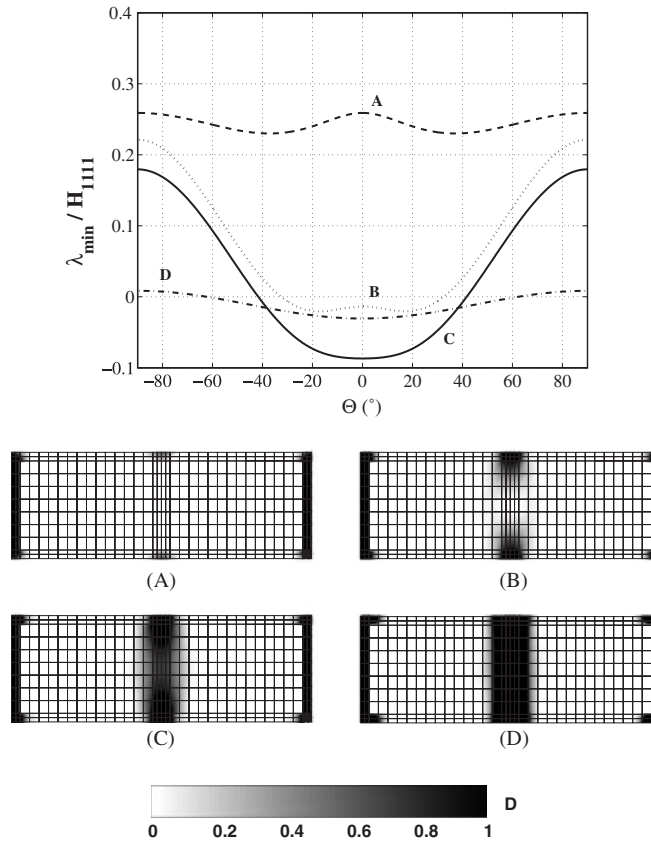


Figure 7. Acoustic tensor eigenspectrum for compression combined with horizontal tension (top) and related damage distributions (bottom). The orientation Θ is defined as the angle between the normal to the potential localization surface and the horizontal direction.

both indicators, i.e. the lowest eigenvalue of 4L_M and of \mathbf{A} , simultaneously indicate the potential for localization.

3.3.2. Vertical compression combined with shear. The eigenvalue data for the case of vertical compression combined with an equal amount of shear are shown in Figures 8 and 9. Initially, the head joint is partially degraded and damage is initiated in parts of the bed joints, as a precursor to the expected staircase crack pattern, Figure 9. However, the damaged segment of the bed joint still contains some undamaged material. This evolution is reflected in the corresponding acoustic tensor eigenspectrum, in which the values are decreasing faster for orientations between $\Theta = 0^\circ$ and $\Theta = 90^\circ$ compared to orientations between $\Theta = -90^\circ$ and $\Theta = 0^\circ$. The lowest eigenvalue of the homogenized tangent stiffness remains positive. This crack pattern continues to evolve as shown in Figure 9, state B and a first minimum of the acoustic tensor eigenspectrum becomes negative for an orientation of $\Theta = 4.1^\circ$. Note that the damaged bed joint segment still contains some undamaged mortar as shown in Figure 9 (state B). The acoustic tensor criterion (19) detects

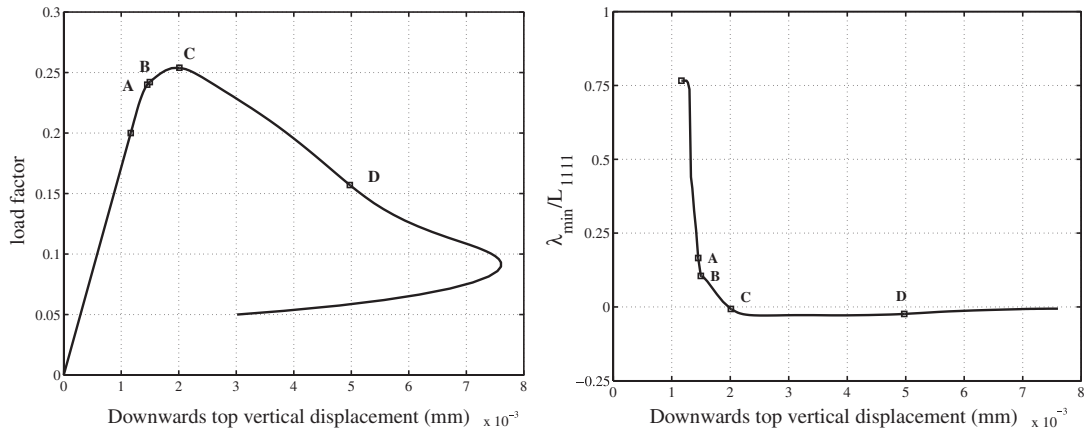


Figure 8. Load factor vs vertical displacement of the top controlling node of the cell for vertical compression combined with shear (left). Evolution of the lowest eigenvalue of the homogenized tangent stiffness (right).

loss of ellipticity at this stage. However, the lowest eigenvalue of the tangent stiffness remains positive as can be seen in Figure 8 (point B). The limit point of the homogenized stress–strain response has not yet been reached, and the load can still be increased since no continuous crack path is formed and periodic boundary conditions are applied (see Section 2.3). Upon further loading, damage spreads over the complete bed joint segment as illustrated for state C, leading to the formation of a staircase crack pattern. This happens when the macroscopic limit point is reached. Simultaneously, a second minimum of the acoustic tensor eigenspectrum becomes negative for an orientation of approximately $\Theta = 58.3^\circ$, see Figure 9, state C. This orientation is close to the averaged crack orientation specified above, the difference being linked to the non-uniform damage distribution inside the damaged zone at this stage. As from this point, the lowest eigenvalue of the homogenized tangent stiffness becomes negative as well, see Figure 8, and both the loss of ellipticity criterion (19) and the limit point condition (20) are now satisfied. The orientation corresponding to this new minimum further evolves towards $\Theta = 53.8^\circ$, which differs by less than 1° from the angle of $\Theta = 54.7^\circ$ predicted by geometric arguments. Localization therefore seems to be best detected from the homogenized tangent via criterion (20), as the average damage pattern orientation appears to be linked to the second bifurcation point detected by the loss of ellipticity criterion (19). This bifurcation point is reached at the limit point in the homogenized response. The minima of the acoustic tensor eigenspectrum first pick up another orientation than the expected orientation. Clearly the first negative minimum of the acoustic tensor eigenspectrum, in the rising part of the averaged stress–strain response, is linked to the non-symmetry of the homogenized tangent stiffness.

3.3.3. Identification and selection of the localization orientation. The obtained results strongly indicate that the localization analysis based on the homogenized tangent stiffness delivers useful information related to the mesostructural evolution inside the unit cell. Based on the above observations, the limit point criterion (20) will be used as an indicator of localization in the sequel

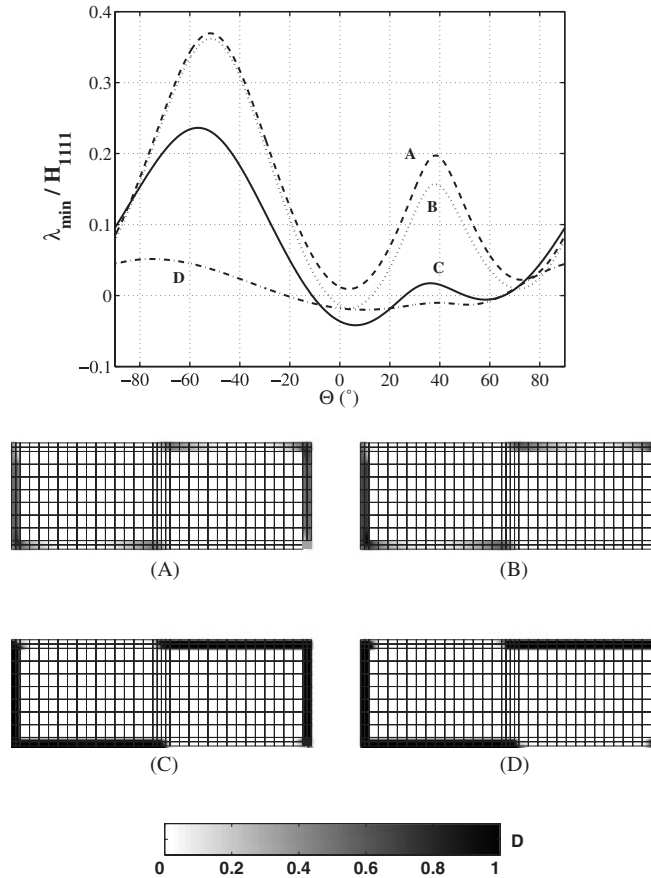


Figure 9. Acoustic tensor eigenspectrum for compression combined with shear (top) and related damage distribution (bottom).

of the paper rather than relation (19). Despite the lack of a rigorous mathematical motivation, the former criterion offers a more efficient way of detecting localization since it is computationally cheaper than the inspection of the acoustic tensor eigenvalues for all possible orientations. Once localization is detected by (20), the orientation associated to the localization will be determined by an eigenspectrum analysis of the acoustic tensor. The orientation corresponding to the negative minimum of the acoustic tensor eigenspectrum, which appeared simultaneously with the limit point, is chosen. Note that (20) is not able to detect bifurcations arising before the limit point. For the shearing-compression case above, the first bifurcation indication obtained from the acoustic tensor is thus ignored. Although the choice for the criterion (20) is in principle pragmatic, it can be further supported by energetic considerations for the shearing-compression loading case, showing that the fundamental homogeneous solution path is more critical than the localized solution at the first bifurcation, see Reference [31].

4. ENHANCED MULTI-SCALE SCHEME FOR MACROSCOPIC LOCALIZATION

4.1. Motivation

The first-order multi-scale technique has to be amended in order to include localization bands as suggested in Section 3. Localization bands in the form of a pair of weak discontinuities embedded in an element were already used in Reference [32] to simulate strain localization in isotropic materials. The proper representation of a true discontinuity, i.e. with complete separation of the crack faces for mode I or mode II opening and proper energy dissipation, requires the use of kinematically enhanced strain fields, see References [33, 34]. This improvement is however only clearly motivated for constant strain elements and does not solve completely the mesh alignment sensitivity, see Reference [35] for a detailed discussion. More advanced discretisation techniques forcing crack path continuity are now available for closed-form constitutive frameworks [35], but their adaptation to multi-scale techniques is not considered in the present contribution.

In the present approach, strain discontinuities defining a localization band are introduced to represent the behaviour of the physical volume associated with a macroscopic sample point (Gauss point) when macroscopic localization is detected. The localization detection is based on the criterion presented in Section 3, whereas the localization width is extracted from the unit cell dimensions along the direction \mathbf{n} given by the localization detection. The material surrounding the localization band is assumed to unload elastically, thus resulting in a discontinuous bifurcation.

4.2. Embedded localization band

In order to include a discontinuous bifurcation in a macroscopic point, an approximate embedded band model is used, based on a relaxed Taylor assumption [36]. The Gauss point volume is split into a localized band (b), and its surrounding, unloading volume (s), see Figure 10. The volume fractions of the band and surrounding material are denoted by f^b and f^s , and the strain jump between the band and surrounding material is defined by the normal to the band \mathbf{n} and the strain jump mode \mathbf{m} . The relaxed Taylor model consists in imposing a constant strain in each sub-region according to

$$\begin{aligned} \mathbf{E}^b &= \mathbf{E} + f^s(\mathbf{m}\mathbf{n})^{\text{sym}} \\ \mathbf{E}^s &= \mathbf{E} - f^b(\mathbf{m}\mathbf{n})^{\text{sym}} \end{aligned} \tag{21}$$

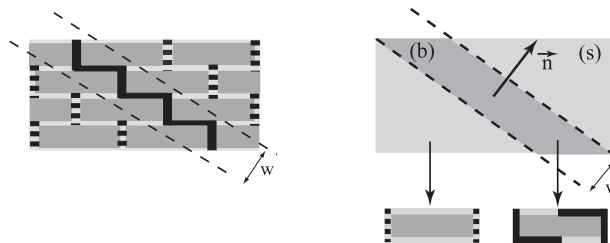


Figure 10. Idealization of the constitutive response for a macroscopic material point using a relaxed Taylor model.

where (\mathbf{mn}) represents the dyadic product of the vectors \mathbf{m} and \mathbf{n} . With these assumptions, the volume-averaged strain is identical to the macroscopically applied strain

$$\mathbf{E} = f^b \mathbf{E}^b + f^s \mathbf{E}^s \quad (22)$$

The stress variations in the two phases are obtained with their respective tangent stiffness

$$\begin{aligned} \delta \Sigma^b &= {}^4 \mathbf{L}_M^b : \delta \mathbf{E}^b \\ \delta \Sigma^s &= {}^4 \mathbf{L}_M^s : \delta \mathbf{E}^s \end{aligned} \quad (23)$$

and the macroscopic stress variation $\delta \Sigma$ is obtained by volume averaging via

$$\delta \Sigma = f^b \delta \Sigma^b + f^s \delta \Sigma^s \quad (24)$$

As is clarified in Figure 10, the assumption is made that the material responses of the band and of its surrounding volume can be deduced from the mesostructure according to the same scale transition as in the initial first-order framework. This clearly introduces an approximation, since this scale transition is based on a (local) periodicity assumption. According to this assumption, a cell within the band behaves as if it were surrounded by identically behaving cells, whereas in the real mesostructure the adjacent cells may be unloading. Similarly, the behaviour of the material outside the band does not take into account the presence of weaker, localizing cells in the band. This assumption may therefore have some influence on the predicted post-peak response, e.g. on the resulting energy dissipation. An improvement could be obtained by using larger periodic cells which include several periods of the mesostructure together with weaker (integral) boundary conditions at their boundaries, but these options clearly require a more extensive treatment. Note also that another limitation of the periodicity is the inability to correctly model the energy dissipation for failure patterns which do not match the initial periodicity of the material. For example, for the case of vertical cracking in running bond masonry (see Figure 7, Section 3.3), the development of two failure zones inside the unit cell may result in an overestimation of the energy dissipation.

4.3. Coupled multi-scale scheme for localized behaviour

Based on the presented assumptions, the first-order multi-scale solution scheme is enhanced in order to capture macroscopic localization. Prior to localization, the multi-scale scheme sketched in Figure 1 is applied. Upon the detection of localization, a band is inserted and the updated scheme illustrated in Figure 11 is initiated. Based on the localization orientation \mathbf{n} and the related volume fractions, the macroscopic strain is decomposed into strains within the band and within its surrounding volume according to (21). The band material response is then evaluated through the first-order multi-scale scheme using a unit cell computation. Since the material surrounding the band is assumed to unload elastically, its secant stiffness ${}^4 \mathbf{L}_M^s$ is evaluated only once. The macroscopic stress is obtained from the averaging relation (24). The determination of the complete macroscopic material response for a given macroscopic load step now consists in solving the following problem: given a macroscopic strain increment $\Delta \mathbf{E}$ and the orientation of the localization band \mathbf{n} , determine (i) the macroscopic stress increment $\Delta \Sigma$ (3 independent unknowns), (ii) the increment of the strain jump $\Delta \mathbf{m}$ (2 unknowns). These unknowns may be determined from the traction continuity requirement at the interface between the band and its surrounding material (2 equations)

$$\mathbf{n} \cdot (\Sigma^b - \Sigma^s) = \mathbf{0} \quad (25)$$

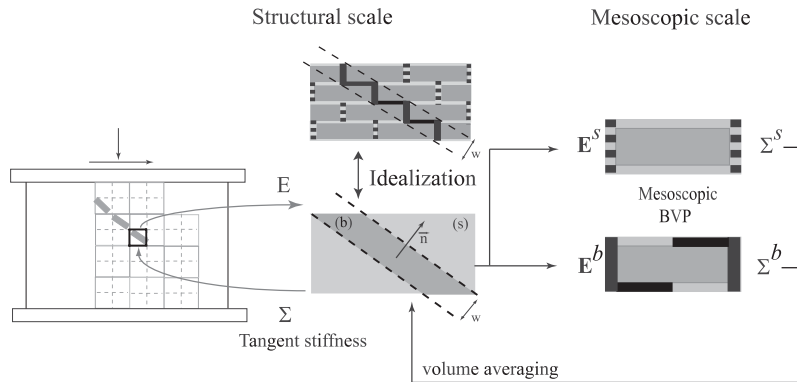


Figure 11. Enhanced first-order multi-scale scheme with embedded strain discontinuity for localized behaviour.

and the stress averaging relation (three equations)

$$\Sigma = f^b \Sigma^b + f^s \Sigma^s \tag{26}$$

It is emphasized that this problem (Equations (25) and (26)) is non-linear, and thus requires an additional iterative solution procedure at the level of a macroscopic sampling point. This becomes apparent by expressing the traction continuity in (25) in terms of the strain increments in the band and the surrounding material as defined in relation (21)

$$n \cdot ({}^4L_M^b - {}^4L_M^s) : \Delta E + n \cdot (f^s {}^4L_M^b + f^b {}^4L_M^s) : (\Delta mn)^{sym} = 0 \tag{27}$$

In relation (27), the tangent material stiffness in the band, ${}^4L_M^b$, is a non-linear function of the strain increment in the band ΔE^b , and thus also of the strain jump increment Δm . As a consequence, three nested solution procedures should *a priori* be used in this enhanced framework: (i) a solution procedure for equilibrium at the macroscopic scale, (ii) a solution procedure to solve the non-linear set of equations of the localization band model, and (iii) a solution procedure at the unit cell level for the solution of the mesostructural boundary value problem.

The orientation of the localization band is not considered as an unknown, but is determined by the localization analysis. As shown in Section 3 for some fundamental equilibrium paths, a rotation of the localization orientation may occur as a result of mesoscopic damage evolution inside the unit cell. This effect is taken into account in order to avoid any stress locking effect at the macroscopic scale. The acoustic tensor associated to the band material tangent is therefore analysed at each converged configuration and the band orientation is updated accordingly. In the current version of the framework, no crack closure effect is included at the macroscopic scale. A localization band cannot be de-activated, and a material point in which a localization band has been inserted is not allowed switch back to a distributed damage pattern.

5. SCALE TRANSITION PROCEDURE FOR LOCALIZED BEHAVIOUR

5.1. Multi-scale solution procedure

The proposed multi-scale scheme involves the numerical solution of equilibrium problems at two scales: the macroscopic or structural scale and the mesostructural scale. When localization is triggered, three sets of equations need to be solved. At the macroscopic scale, the global equilibrium problem can be written in the usual way

$$\nabla_M \cdot \boldsymbol{\Sigma} + \mathbf{F} = \mathbf{0} \quad (28a)$$

$$\boldsymbol{\Sigma} = F_{\Sigma}(\mathbf{E}) \quad (28b)$$

where F_{Σ} denotes the numerically obtained response of the embedded band model. The decomposition of the material behaviour in a band and its surrounding material is characterized by the following set of equations:

$$n \cdot (\boldsymbol{\Sigma}^b - \boldsymbol{\Sigma}^s) = \mathbf{0} \quad (29a)$$

$$\boldsymbol{\Sigma} = f^b \boldsymbol{\Sigma}^b + f^s \boldsymbol{\Sigma}^s \quad (29b)$$

$$\mathbf{E}^b = \mathbf{E} + f^s (\mathbf{m}\mathbf{n})^{(\text{sym})} \quad (29c)$$

$$\mathbf{E}^s = \mathbf{E} - f^b (\mathbf{m}\mathbf{n})^{(\text{sym})} \quad (29d)$$

$$\boldsymbol{\Sigma}^b = F_{\Sigma^b}(\mathbf{E}^b) \quad (29e)$$

$$\boldsymbol{\Sigma}^s = F_{\Sigma^s}(\mathbf{E}^s) \quad (29f)$$

At the mesoscopic scale, the equilibrium problem and the additional averaging equation have to be solved together with the related boundary conditions

$$\nabla_m \cdot \boldsymbol{\sigma} = \mathbf{0} \quad (30a)$$

$$\bar{\varepsilon}_{\text{eq}} - l_c^2 \nabla^2 \bar{\varepsilon}_{\text{eq}} = \varepsilon_{\text{eq}} \quad (30b)$$

Equations (30a) and (30b) are solved iteratively for each iteration of the macroscopic solution procedure.

The multi-scale solution procedure as discussed so far implicitly assumes that a solution of the mesostructural problem and of the embedded band model always exists for a given macroscopic strain \mathbf{E} . This condition is not satisfied when the average response exhibits a snap-back, which requires adaptations in the scale transition procedures.

5.2. Causes of snap-back in averaged material response

Snap-back is a structural phenomenon appearing when localization of damage occurs in zones which are narrow with respect to the structural size. Energetically, it occurs when the rate at which the elastic zone releases elastically stored energy becomes larger than the rate at which energy is consumed by the degradation of the softening material. This calls for adequate path following

techniques [30]. Such methods use a generalized load control, in which a scalar load factor constitutes an additional unknown. To solve the set of equations, a constraint equation is added, in terms of the conventional degrees of freedom of the structure and the load factor. A monotonically increasing quantity is used to define the constraint and hence to control the computation. For problems involving damage localization in narrow zones, local constraints (involving only degrees of freedom related to the damage process zone itself) have been shown to perform better than global constraints [30].

The macroscopic material point response is obtained here from a mesostructural computation. This implies that the average response may also show snap-back, since relatively brittle mesostructural materials are considered and damage growth tends to localize in the weaker and relatively narrow mortar joints. If classical non-linear displacement-based finite element procedures are used at the macroscopic scale, it is implicitly assumed that for a given strain increment a resulting stress can always be determined, i.e. that the mesostructural boundary value problem always possesses a solution for the prescribed macroscopic strain increment. This is clearly not true for strains beyond a snap-back point, and a macroscopic displacement-based multi-scale scheme may hence fail in capturing the macroscopic equilibrium path.

A second potential source of snap-back of the deduced macroscopic material response is formed by the averaging relations of the localization band model, i.e. Equations (29b)–(29d). These relations take into account localization bands with a characteristic volume that is smaller than the volume associated with the Gauss point where the macroscopic material behaviour is sampled. Since this band is behaving in a quasi-brittle manner and the remaining material is assumed to unload elastically, the overall macroscopic material response may show snap-back, even if the average behaviour of the band unit cell does not. This type of snap-back is more likely to occur for relatively coarse meshes, in which the damage band is thin compared with the volume associated to the Gauss points.

5.3. Treatment of mesostructural snap-backs

To be able to handle mesostructural snap-backs in the proposed multi-scale solution scheme, two difficulties need to be solved. First, the macroscopic solution procedure must be able to predict a decreasing macroscopic strain increment as from the strain control limit point. Secondly, in the snap-back regime, either the elastic unloading or the dissipative equilibrium path will be followed for a given negative strain increment. To avoid the selection of the former, the scale transition procedure should apply a decreasing macroscopic strain to the mesostructure, along with an additional condition that steers the solution onto a dissipating path.

5.3.1. Strain jump control for embedded band snap-back. Let us assume that a localization band was introduced in the considered material volume (relations (29a)–(29f)), and that the homogenized unit cell response does not exhibit snap-back. Given the small width of the band and the brittleness of its behaviour, a snap-back may appear in the averaged response of the finite volume associated to the considered macroscopic material point.

The kinematic variable which characterizes the strain jump between the band and the surrounding material is the vector \mathbf{m} . If the band material follows a softening branch while the surrounding unloads, the strain jump $(\mathbf{m}\mathbf{n})^{\text{sym}}$ should increase, even if the overall material response exhibits snap-back. To enforce further dissipation in the material, the macroscopic solution procedure should thus enforce the growth of \mathbf{m} .

A way to enforce this condition is to impose on the localization band model a positive increment of the strain jump vector \mathbf{m} . The vector \mathbf{m} is therefore defined as a variable at the macroscopic level in each macroscopic Gauss point. Since Equation (29a) is non-linear, simultaneously imposing a strain jump \mathbf{m} and a macroscopic strain \mathbf{E} does not automatically lead to an equilibrium configuration. An equivalent number of equations conjugate with these unknowns must be formulated at the macroscopic level and solved at this scale. The traction continuity requirement between the band and surrounding material (29a) may be used for this purpose. This equation couples the strain jump to the macroscopic displacement field through the components of the macroscopic strain tensor, as shown by relation (27). Due to the non-linear nature of (27), the prescribed values of the strain jump \mathbf{m} and the applied overall strain \mathbf{E} will generally not lead to an equilibrium state immediately, meaning that traction continuity will not be directly satisfied for the prescribed \mathbf{m} . Equation (29a) therefore has to be solved iteratively, together with the discrete macroscopic equilibrium equations which result from (28a). This means that the traction continuity between the band and the surrounding phases (29a) is only satisfied in macroscopically converged configurations, and not in the intermediate iterative steps.

5.3.2. Dissipation control for unit cell snap-back. As illustrated in Reference [37], the averaging of the unit cell behaviour may cause mesostructural snap-back in the response of the localization band itself. In order to follow the dissipative equilibrium path of the cell, an additional condition related to mesoscopic dissipation inside the cell must be added to the governing equations which are prescribed to the mesostructural boundary value problem by the macroscopic solution procedure, as proposed in Reference [37]. The principle of this technique is briefly recalled for the sake of clarity. Assuming a discontinuous bifurcation upon appearance of the band, the surrounding material unloads elastically, and an enhancement is only needed for the unit cell computation associated to the localization band. A variable related to the dissipating damage process zone—here, a non-local equivalent strain field degree of freedom that drives the mesoscopic damage growth—can be imposed by the macroscopic solution procedure to the cell to force the solution onto a dissipative path. This non-local degree of freedom must therefore be transferred to the macroscopic scale, and a conjugate equation has to be solved iteratively at this scale.

The ‘external’ prescription of a non-local strain in the cell gives rise to a conjugate reaction ‘force’, or conjugate residual $f_{\bar{\varepsilon}}$. This residual can be interpreted as the external action needed to enforce the prescribed value of the non-local strain increment $\Delta\bar{\varepsilon}$ on top of the imposed average strain \mathbf{E} . Since in reality no such external action exists, it should vanish in the equilibrium state:

$$f_{\bar{\varepsilon}} = 0 \quad (31)$$

Rather than using this condition at the mesoscopic scale—which would be equivalent with not prescribing $\Delta\bar{\varepsilon}$ —it is transferred to the macroscopic set of equations. This allows to have more control on the mesoscopic equilibrium iterations, thereby still satisfying the original equilibrium equations in the final macroscopically converged solution. This feature allows to pass strain control limit points of the homogenized stress–strain behaviour, and, since it selects the corresponding tangent stiffness, to follow the snap-back dissipative solution.

For the practical implementation of this enhanced control of the mesoscopic dissipation, the reader is referred to Reference [37]. Note that the non-local degree of freedom may already be introduced in the macroscopic description at the start of the computation, as it does not have any effect in the pre-localized regime.

An essential difference with the treatment of snap-back due to the macroscopic localization band discussed in Section 5.3.1 resides in the fact that the selection of the non-local degree of freedom which is used to enforce dissipation at the cell level should evolve as a result of mesoscopic damage evolution. The non-local degree of freedom corresponding to the largest incremental damage growth is selected at the end of each macroscopic increment as the controlling variable of a given unit cell in the subsequent increment. Note that the procedure described here is rather general. If another type of model is used at the meso-scale, e.g. a cohesive zone approach, the solution control can also be based on a relative displacement between two nodes, or even other quantities like the dissipated energy, as suggested in Reference [38].

6. COMPUTATIONAL ASPECTS OF THE ENHANCED MULTI-SCALE SCHEME

6.1. Governing equations in macroscopic and mesoscopic solution procedures

As a result of the enhancements introduced in order to handle mesostructural snap-backs, mesostructural equations are incorporated in the macroscopic solution procedure. The governing equations and the level at which they are solved are summarized in Table II, and the corresponding scale transition procedure is represented in Figure 12. The essential difference with the scheme presented in Figure 11 resides in the presence of a set of mesoscopic non-local degrees of freedom in the macroscopic solution procedure. The band orientation is adapted at the start of each step, based on the evaluation of the tangent operator in the previous converged state. In case the band unit cell response undergoes mesostructural snap-back, its tangent stiffness becomes positive-definite, and no localization direction can be determined anymore, in which case the orientation is fixed.

6.2. Extraction of consistent tangent stiffness for unit cell snap-back control

The fact that a mesoscopic degree of freedom is now included in the set of unknowns at the macroscopic level means that the extraction of the macroscopic tangent operator presented in Reference [39] must be adapted as well. This tangent now consists of four tensors which relate variations of the stress Σ and the non-local residual $f_{\bar{\epsilon}}$ to variations of the strain \mathbf{E} and of the non-local variable $\bar{\epsilon}$ according to

$$\delta \Sigma = {}^4 C_M^{uu} : \delta \mathbf{E} + C_M^{ue} \delta \bar{\epsilon}, \quad \delta f_{\bar{\epsilon}} = C_M^{eu} : \delta \mathbf{E} + C_M^{ee} \delta \bar{\epsilon} \tag{32}$$

Table II. Distribution of the field governing equations among the different solution procedures in the enhanced first-order scheme.

Solution level	Equations	Physical meaning	Unknowns
Macroscopic	(28a)	Macro-equilibrium	Displacement field \mathbf{u} (macroscopic variation)
	(29a)	Traction continuity	Strain discontinuities \mathbf{m}
	(31)	Non-local residual	Mesoscopically prescribed $\bar{\epsilon}_{eq}$
Mesoscopic	(30a)	Mesoscopic equilibrium	Displacement field \mathbf{u} (mesoscopic variation)
	(30b)	Non-local averaging	Non-local field $\bar{\epsilon}_{eq}$

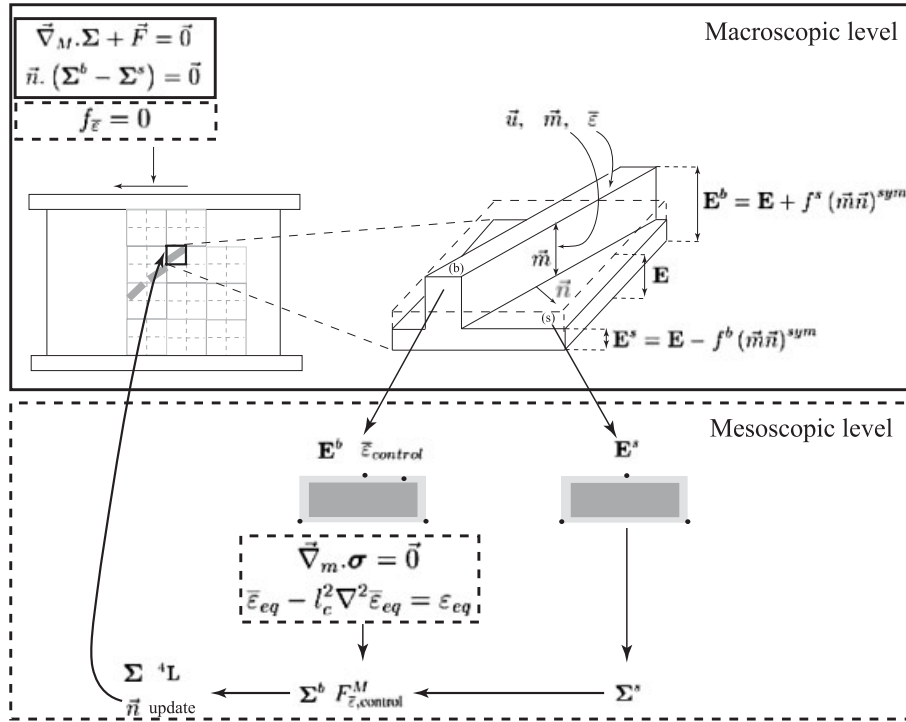


Figure 12. Principles of the localization-enhanced first-order scheme with nested macroscopic and mesoscopic solution procedures and with mesostructural snap-back handling. The upper part of the figure represents the structural part, including localization band at the level of Gauss point volumes, the lower part represents the mesoscopic unit cell computations.

The tangent stiffness relation of the mesostructural problem condensed towards the control displacements and the controlling non-local degree of freedom reads in matrix format

$$\begin{bmatrix} [\mathbf{K}_M^{uu}] & \{\mathbf{K}_M^{ue}\} \\ \langle \mathbf{K}_M^{eu} \rangle & \mathbf{K}_M^{ee} \end{bmatrix} \begin{Bmatrix} \{\delta u_M\} \\ \delta \bar{\epsilon} \end{Bmatrix} = \begin{Bmatrix} \{\delta f_M\} \\ \delta f_{\bar{\epsilon}} \end{Bmatrix} \quad (33)$$

When expressed in tensorial format, this relation can be reworked to obtain the following expressions for the consistent tangent as shown in Reference [37]:

$${}^4\mathbf{C}_M^{uu} = \frac{1}{V_{\text{cell}}} \left(\sum_{n=1}^3 \sum_{p=1}^3 \mathbf{x}^{(n)} \mathbf{K}_M^{uu(np)} \mathbf{x}^{(p)} \right)^{(rs)}, \quad \mathbf{C}_M^{ue} = \frac{1}{V_{\text{cell}}} \left(\sum_{n=1}^3 \mathbf{x}^{(n)} \mathbf{K}_M^{ue(n)} \right) \quad (34a)$$

$$\mathbf{C}_M^{eu} = \frac{1}{V_{\text{cell}}} \left(\sum_{p=1}^3 \mathbf{K}_M^{eu(p)} \mathbf{x}^{(p)} \right)^{(rs)}, \quad \mathbf{C}_M^{ee} = \mathbf{K}_M^{ee} \quad (34b)$$

The consistent tangent operator ${}^4\mathbf{C}_M^{uu}$ defined by relations (34a) is not the material tangent in the usual sense, due to the presence of additional information related to the mesoscopic non-local

degree of freedom $\bar{\varepsilon}$. Upon macroscopic convergence, the unit cell is in equilibrium under the prescribed macroscopic strain increment and the residual $f_{\bar{\varepsilon}}$ vanishes, and the material tangent operator may then be recovered as

$${}^4\mathbf{L}_M = {}^4\mathbf{C}_M^{uu} - \frac{1}{\mathbf{C}_M^{ee}} \mathbf{C}_M^{ue} \mathbf{C}_M^{eu} \tag{35}$$

for the detection or update of the localization orientation.

6.3. Discretization and linearization of the macroscopic solution procedure

A nested finite element scheme is used in order to solve the governing equations according to the scheme given in Table II. To achieve this, unknowns related to the following kinematic variables have to be defined in the macroscopic solution procedure: (i) the displacement field \mathbf{u} , (ii) the strain jump vector \mathbf{m} in each quadrature point where bifurcation has occurred, and (iii) a mesoscopic non-local strain degree of freedom $\bar{\varepsilon}$ in each quadrature point. Two unknowns related to the strain jump \mathbf{m} and one related to $\bar{\varepsilon}$ are thus defined in each integration point. The displacement field is interpolated by conventional finite element shape functions. Note that the piecewise uniform strain state assumed in the localization band model is only consistent with the finite element interpolation of the displacements in case constant strain triangle elements are used. This restriction is also present in ‘classical’ embedded discontinuity elements available in the literature, the formulation of which is usually well motivated only for constant strain elements [35].

Using the finite element displacement interpolation, the discretized form of the governing equations at iteration (k) is given in matrix format by

$$\int_V [\mathbf{B}]^T \{\boldsymbol{\Sigma}^{(k)}\} dV = \{\mathbf{f}_{\text{ext}}^{(k)}\} \tag{36}$$

$$[n](\{\boldsymbol{\Sigma}^{\text{b},(k)}\} - \{\boldsymbol{\Sigma}^{\text{s},(k)}\}) = \{0\} \tag{37}$$

$$f_{\bar{\varepsilon}}^{(k)} = 0 \tag{38}$$

where $[\mathbf{B}]$ is the matrix which links the interpolated macroscopic strain field to the macroscopic nodal displacements, and $[n]$ is a matrix containing the components of the normal to the localization band. The integral in (36), is defined on the entire structure. Equations (37) and (38) are formulated for each quadrature point where the macroscopic material behaviour is sampled. Relations (36)–(38) are next linearized using (δ denotes an iterative update of a quantity)

$$\{\boldsymbol{\Sigma}^{(k)}\} = \{\boldsymbol{\Sigma}^{(k-1)}\} + \{\delta\boldsymbol{\Sigma}\} \tag{39}$$

$$\{\mathbf{m}^{(k)}\} = \{\mathbf{m}^{(k-1)}\} + \{\delta\mathbf{m}\} \tag{40}$$

$$\bar{\varepsilon}^{(k)} = \bar{\varepsilon}^{(k-1)} + \delta\bar{\varepsilon} \tag{41}$$

6.3.1. Macroscopic equilibrium equation. The macroscopic stress variation in a given quadrature point may be obtained using the stress averaging on the localization band and the remaining material according to (29b), in which the band and the surrounding responses (29e) and (29f) are

substituted, and in which (32) is used for the band. If $[\mathbf{L}^s]$ contains the components of the secant stiffness in the surrounding material, one obtains

$$\{\delta\boldsymbol{\Sigma}\} = f^b([\mathbf{C}_M^{uu}]\{\delta\mathbf{E}^b\} + [\mathbf{C}_M^{ue}]\delta\bar{\boldsymbol{\varepsilon}}) + f^s[\mathbf{L}_M^s]\{\delta\mathbf{E}^s\} \quad (42)$$

Expressing the strains in the band and in the surrounding material in terms of the strain discontinuity through (29c) and (29d), and introducing the finite element interpolation for the macroscopic strain \mathbf{E} , the variation of stress is given as

$$\{\delta\boldsymbol{\Sigma}\} = (f^b[\mathbf{C}_M^{uu}] + f^s[\mathbf{L}_M^s])[\mathbf{B}]\{\delta u\} + f^b f^s([\mathbf{C}_M^{uu}] - [\mathbf{L}_M^s])[n]\{\delta m\} + f^b[\mathbf{C}_M^{ue}]\delta\bar{\boldsymbol{\varepsilon}} \quad (43)$$

where the matrix $[n]$ is defined such that its multiplication with $\{\delta m\}$ yields the symmetric part of $n\delta m$. Note that in this equation, the first term connects the macroscopic displacement degrees of freedom of the considered macroscopic finite element, whereas the remaining terms relate to variations of variables which are local to the considered quadrature point. Substituting (39) and (43) in the discretized macroscopic equilibrium (36) yields

$$[\mathbf{K}_{uu}]\{\delta u\} + \sum_{(i)} ([\mathbf{K}_{um,(i)}]\{\delta m_{(i)}\} + \{\mathbf{K}_{ue,(i)}\}\delta\bar{\boldsymbol{\varepsilon}}_{(i)}) = \{\mathbf{f}_{\text{ext}}^{(k)}\} - \{\mathbf{f}_{\text{int}}^{(k-1)}\} \quad (44)$$

where

$$[\mathbf{K}_{uu}] = \int_V [\mathbf{B}]^T (f^b[\mathbf{C}_M^{uu}] + f^s[\mathbf{L}_M^s])[\mathbf{B}] dV \quad (45)$$

$$[\mathbf{K}_{um,(i)}] = V_{(i)} f^b f^s [\mathbf{B}]^T ([\mathbf{C}_M^{uu}] - [\mathbf{L}_M^s])[n] \quad (46)$$

$$\{\mathbf{K}_{ue,(i)}\} = V_{(i)} f^b [\mathbf{B}]^T \{\mathbf{C}_M^{ue}\} \quad (47)$$

and $\{\mathbf{f}_{\text{ext}}^{(k)}\}$ are the external nodal forces in iteration (k) . The sum over the Gauss points indicated by the index i in this relation reflects that the strain jump unknowns and the mesoscopic non-local strain unknowns are associated to these points. All terms in (46) and (47) are evaluated at the considered Gauss points and $V_{(i)}$ denotes the volume associated with the considered Gauss point by the quadrature scheme.

6.3.2. Traction continuity across the localization band. Traction continuity across the boundary of the localization band in a given Gauss point volume, as expressed by Equation (37), can be linearized using similar substitutions as above. This leads to the following linearized equation for iteration (k) :

$$[\mathbf{K}_{mu}]\{\delta u\} + [\mathbf{K}_{mm}]\{\delta m\} + \{\mathbf{K}_{me}\}\delta\bar{\boldsymbol{\varepsilon}} = -[n](\{\boldsymbol{\Sigma}^{b,(k-1)}\} - \{\boldsymbol{\Sigma}^{s,(k-1)}\}) \quad (48)$$

with the corresponding stiffness matrices defined as

$$[\mathbf{K}_{mu}] = [n]([\mathbf{C}_M^{uu}] - [\mathbf{L}_M^s])[\mathbf{B}] \quad (49)$$

$$[\mathbf{K}_{mm}] = [n](f^s[\mathbf{C}_M^{uu}] - f^b[\mathbf{L}_M^s])[n] \quad (50)$$

$$\{\mathbf{K}_{me}\} = [n]\{\mathbf{C}_M^{ue}\} \quad (51)$$

6.3.3. *Non-local residual equation.* Finally, the linearization of Equation (38) is obtained by substituting the expression of the band strain (29c) into the expression of the non-local residual variation (32), yielding for iteration (k)

$$\langle \mathbf{K}_{eu} \rangle \{ \delta u \} + \langle \mathbf{K}_{em} \rangle \{ \delta m \} + \mathbf{K}_{ee} \delta \bar{\epsilon} = - f_{\bar{\epsilon}}^{(k-1)} \tag{52}$$

with

$$\langle \mathbf{K}_{eu} \rangle = \langle \mathbf{C}_M^{eu} \rangle [\mathbf{B}] \tag{53}$$

$$\langle \mathbf{K}_{em} \rangle = f^s \langle \mathbf{C}_M^{eu} \rangle [n] \tag{54}$$

$$\mathbf{K}_{ee} = \mathbf{C}_M^{ee} \tag{55}$$

6.4. *Introduction of localization bands upon material bifurcation*

When localization is detected, a branch switching procedure is used to force the integration point onto the localizing path. In the first increment after localization detection, separate responses of the band and surrounding material are evaluated in the considered macroscopic material point. Based on the detected localization orientation \mathbf{n} , a branch switching procedure is applied to force the appearance of a strain jump $(\mathbf{m}\mathbf{n})^{\text{sym}}$ between the band and the surrounding material. The vector \mathbf{m} is unknown, and no estimate for it is available from the previous increment. A predictor for \mathbf{m} can be obtained from the discontinuous bifurcation assumption. The rate of the vector \mathbf{m} must satisfy the linearized form of the traction continuity (29a)

$$(\mathbf{n} \cdot {}^4\mathbf{L}_M^b \cdot \mathbf{n}) \cdot \dot{\mathbf{m}} = \mathbf{n} \cdot ({}^4\mathbf{L}_M^s - {}^4\mathbf{L}_M^b) : \dot{\mathbf{E}} \tag{56}$$

where ${}^4\mathbf{L}_M^b$ denotes the tangent stiffness in the band and ${}^4\mathbf{L}_M^s$ the tangent stiffness in the remaining material. Initially, the latter is taken equal to the secant stiffness, whereas the tangent stiffness before bifurcation is used as an initial estimate for ${}^4\mathbf{L}_M^b$. Since the direction \mathbf{n} has been determined by the localization condition, Equation (56) can be used to determine a predictor of the finite increment $\Delta \mathbf{m}$ which is consistent with the finite increment of the overall strain $\Delta \mathbf{E}$. This estimate is only an approximation since finite increments are estimated from the linearized equation and since the tangent stiffness before the bifurcation is used as an estimate for the band. With this strain jump prediction $\Delta \mathbf{m}$, the band strain increment may be predicted as

$$\Delta \mathbf{E}^b = \Delta \mathbf{E} + f^s (\mathbf{n} \Delta \mathbf{m})^{\text{sym}} \tag{57}$$

So far, the prediction of the non-local degree of freedom increment $\Delta \bar{\epsilon}$ available from the macroscopic solution procedure does not take into account the branching at the bifurcation point, since it still relates to the overall strain increment $\Delta \mathbf{E}$. A new prediction of $\Delta \bar{\epsilon}$ thus has to be obtained, related to the strain increment $\Delta \mathbf{E}^b$ applied to the band rather than to $\Delta \mathbf{E}$. This new prediction of the non-local degree of freedom may be obtained from relation (52) by setting the non-local residual increment $\Delta f_{\bar{\epsilon}}$ to zero. A correction for $\Delta \bar{\epsilon}$ which takes into account the appearance of the strain jump is obtained as

$$\Delta \bar{\epsilon} = \frac{-1}{\mathbf{K}_{ee}} [\langle \mathbf{K}_{eu} \rangle \{ \Delta u \} + \langle \mathbf{K}_{em} \rangle \{ \Delta m \}] \tag{58}$$

7. APPLICATIONS

In this section, the numerical multi-scale framework developed above is applied to a number of test problems. A simple test case is considered with homogeneous loading at the macroscopic scale in order to illustrate the capability of the algorithm to treat mesostructural snap-back and its sensitivity to the size of the mesostructure. Next, a structural shear wall application is presented to assess the ability of the model to reproduce complex structural failure modes.

7.1. Mesostructural snap-back in a tension-compression test

7.1.1. *Homogeneous solution path.* As shown in Reference [37], the multi-scale framework can be applied to trace the homogenized response where mesostructural unit cell snap-back occurs. If a unit cell is considered to be a part of a structure within the nested multi-scale scheme, the unit cell computation is strain-driven and the snap-back control technique developed in Section 5 is required. To illustrate this, a macroscopic ‘structure’ is tested which consists of a single finite element under homogeneous macroscopic loading, with the same response for all Gauss points. The bifurcation detection and branching are not activated in this computation to ensure that the unit cell response is the only possible cause of snap-back in the homogenized material response. The structure is proportionally stressed with vertical compression combined with horizontal tension along the stress path $(\Sigma_{xx}, \Sigma_{yy}, \Sigma_{xy}) = (0.2, -1, 0)$. The macroscopic ‘structural’ dimensions are taken such that the volume associated to each Gauss point by the quadrature scheme is identical to that of the unit cell, which has the same dimensions as in Section 3.3. The macroscopic finite element has a biquadratic serendipity displacement interpolation and four Gauss points. The damage criteria and material properties used for the constituents are taken from Reference [23]. The load factor evolution is represented in Figure 13 as a function of the top vertical displacement of the structure divided by the number of unit cells along the height of the structure. This curve shows that the unit cell snap-back occurs and is correctly dealt with by the dissipation-enhanced scale transition. For each point of the load–displacement curve marked by a capital letter, the damage state inside the unit cell is depicted in Figure 13. The node used for the dissipation control in each increment is

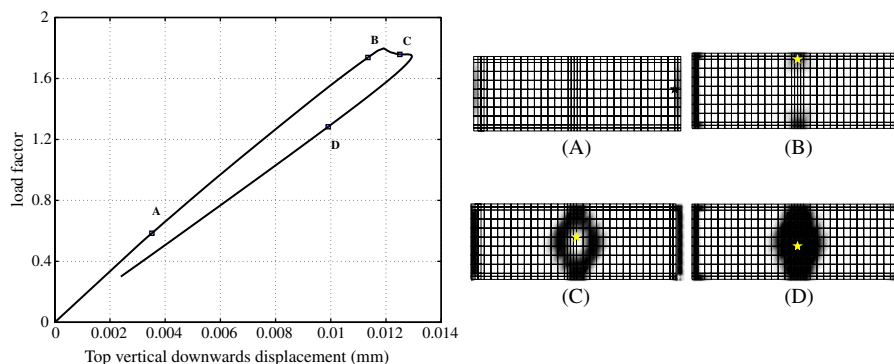


Figure 13. Load–displacement curve and damage distribution obtained by the multi-scale modelling for homogeneous macroscopic tension-compression loading. Each damage distribution corresponds to the point denoted in the load–displacement curve. The stars in the damage distributions indicate the degree of freedom which is selected for the snap-back control in the next increment, after Massart *et al.* [37].

identified by a star. At each stage, these selected nodes are clearly positioned where the incremental damage growth is highest.

7.1.2. *Localized solution within a one-element test.* The analysis can be repeated with a macroscopic ‘structure’ of modified dimensions $600 \times 300 \text{ mm}^2$. Only one macroscopic finite element is again used, which means that the volume associated to each Gauss point by the quadrature scheme is now larger than the unit cell dimensions. The macroscopic loading is kept homogeneous such that all Gauss points will exhibit the same behaviour. For this test, the homogeneous structural solution without localization is compared with the one in which the material response is allowed to localize simultaneously in all Gauss points, i.e. the solution in which part of every Gauss point volume is allowed to unload once the bifurcation condition is satisfied. The predicted localization bands have a vertical orientation, corresponding to the final damage pattern. The effect of the localization band clearly appears in the load–displacement curve in Figure 14, where a sharper snap-back is found for the localized solution. A non-symmetric damage pattern is observed in the cell for the localized solution, due to the use of the non-local strain control in the multi-scale procedure. As illustrated in Figure 14, joint and brick damage is initiated in a symmetric fashion prior to localization. This symmetry causes a bifurcation to appear at the mesoscopic level. This meso-scale bifurcation is not detected in the stress-controlled, direct unit cell computation which therefore shows a symmetric response. When the enhanced multi-scale technique is used together with the branching procedure for the band introduction, the unit cell dissipation control selects one non-local strain degree of freedom for controlling the unit cell even if its symmetric counterpart

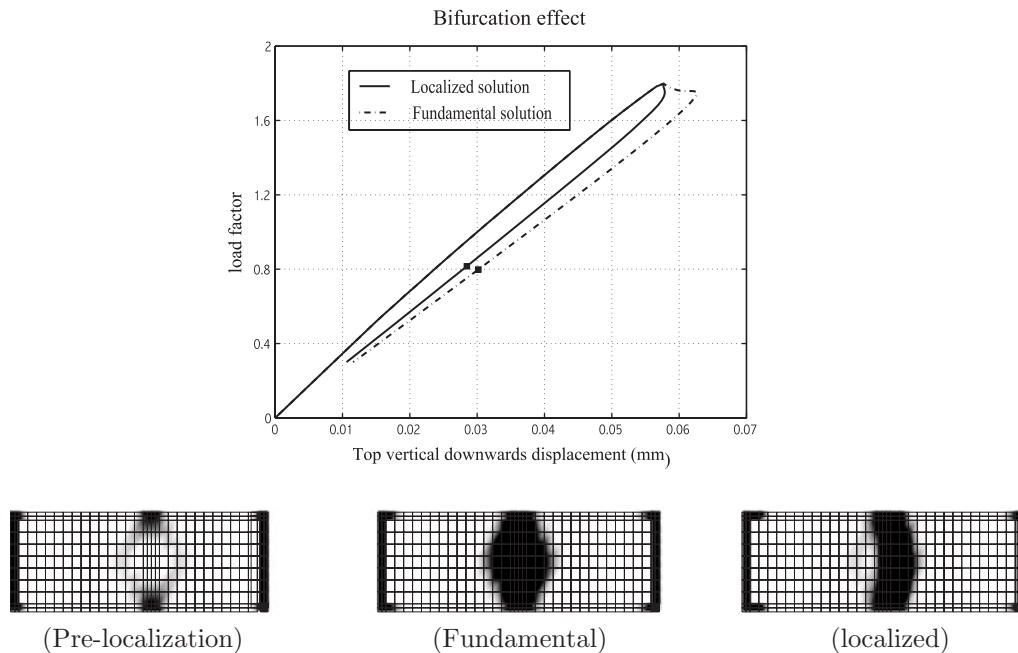


Figure 14. Load–displacement curves and damage distribution obtained by multi-scale modelling for macroscopic tension-compression loading for fundamental and localized solutions.

would be equally suitable. As a consequence, the asymmetric solution in which the selected node continues to be damaged is followed. The sharper snap-back observed in Figure 14 is thus caused not only by the presence of the localization band in each Gauss point, but also by the occurrence of a different mesoscopic damage pattern inside the unit cell.

7.2. Size effect in shear-compression test

As a second elementary test, a single macroscopic element is subjected to vertical compression combined with shear as in Section 3. The influence of the ratio between the structural and the mesostructural dimensions is examined. Since the mesostructural size enters the macroscopic computation via the localization bandwidth, a size effect is observed at the macroscopic scale. If the ratio between the structural dimension and the unit cell dimension increases, a more brittle structural post-peak response is expected since the volume in which energy is dissipated becomes smaller compared to the structural size. To show this effect, the vertical compression-shearing test is repeated with the same unit cell dimensions, but with two different structural dimensions, namely $800 \times 800 \text{ mm}^2$ and $1600 \times 1600 \text{ mm}^2$. Figure 15 shows the load factor versus the displacement, normalized by the structural size, for both structural dimensions together with the structural fundamental paths. For a fixed unit cell size, a larger structure indeed clearly leads to a more brittle structural response.

7.3. Masonry shear wall test

Data related to large-scale tests on masonry structures is scarce in the literature because of the practical difficulties associated with such experiments. Confined shear wall tests are the most commonly used structural experiments [40]. Similar experimental results were already used in Reference [41] for the validation of a discrete mesoscopic masonry model. For practical reasons, the tested structures usually consist of only a few bricks. Since the scale separation between the

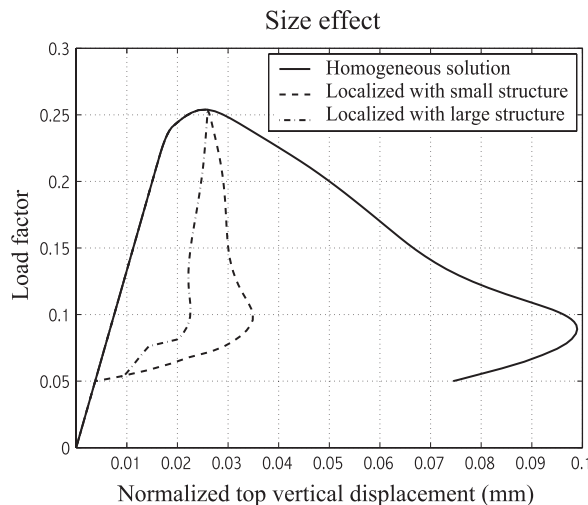


Figure 15. Load–displacement curve for vertical compression combined with shear for two different structural dimensions and a fixed unit cell size.

structural and mesoscopic scales remains intrinsically small in such panels, the corresponding results cannot be used for the quantitative validation of homogenization-based models. However, given the lack of experimental data on large-scale structures, the small-scale test data are nevertheless used here for a *qualitative* assessment of the multi-scale modelling. The type of test reported in Reference [40] for shear walls with openings are considered for this purpose, with altered mesoscopic and macroscopic dimensions for the multi-scale approach to remain applicable. The dimensions of the opening are also modified with respect to the dimensions of the wall.

7.3.1. Problem definition and qualitative description of the experimental response. The wall geometry considered in the simulation is shown in Figure 16. It consists of a plane masonry wall of dimensions $2500 \times 3000 \times 100 \text{ mm}^3$. An opening with dimensions $800 \times 1200 \text{ mm}^2$ is present in the wall. The geometry is slightly non-symmetric in order to trigger an asymmetric response. The totality of bricks consistent with the mesoscopic and structural dimensions is shown in Figure 16 in order to emphasize the costly character of a complete fine-scale modelling of this structure. In the experiments reported in Reference [40], the top and bottom boundaries of the wall were ‘clamped’ in steel beams. The loading is applied in two phases. In a first phase, the wall is compressed by a vertical distributed load applied to the top beam, resulting in a uniform vertical displacement of the top boundary. In the second loading phase, the vertical displacement of the top boundary is fixed and a horizontal shearing force is applied. Here, the effect of the loading set-up is represented by two bands of elements with elastic behaviour. The vertical displacement of the top boundary is forced to remain uniform to simulate the presence of a steel beam. In order to represent the (imperfect) clamping of the wall in the steel beam, a lower stiffness is assumed for the two rows of elastic elements. The shearing load is applied as a distributed load on the right side of this row of elements.

Experimentally, a complex crack evolution pattern was obtained. The average crack pattern stages are illustrated in Figure 17, after [40]. Damage was first initiated with diagonal cracks starting at corners of the opening and in the middle of its top border (Figure 17(a)). These specific damage initiation locations were linked to the small number of bricks in the specimen (the opening

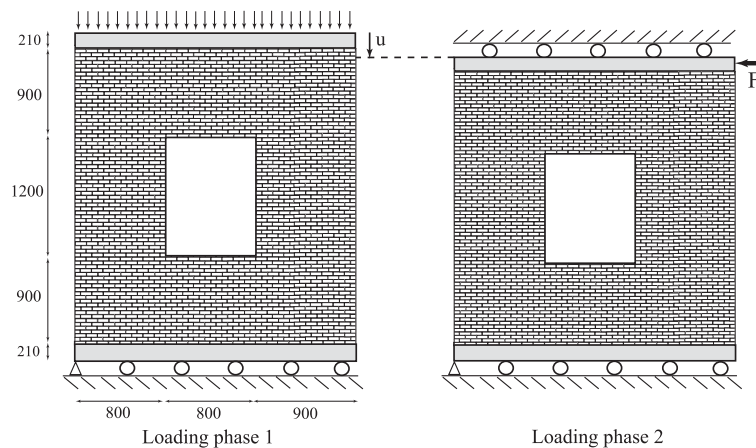


Figure 16. Shear test on a wall with opening: two-phase loading and dimensions.

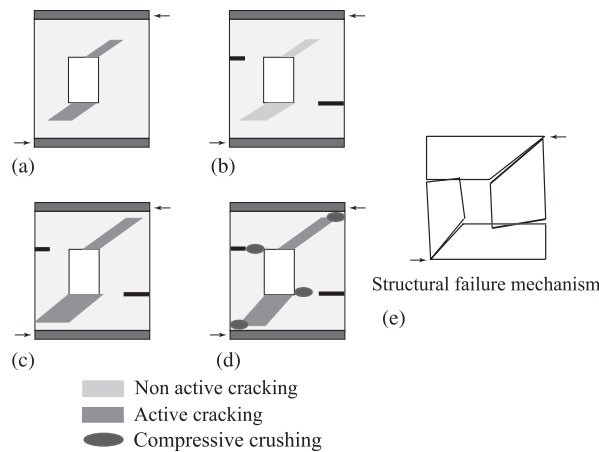


Figure 17. Shear test on a wall with opening—successive cracking states observed in experiments [40].

in the wall had a width of approximately one brick). Shortly after their initiation, these diagonal cracks became inactive, upon the appearance of two tensile horizontal cracks at the free boundaries, Figure 17(b). Later, these horizontal cracks were arrested and two of the diagonal cracks were re-activated and propagated towards the top right and bottom left corners of the wall (Figure 17(c)). Finally, a structural failure mechanism was reached with compressive crushing of two corners of the wall and of two corners of the opening ahead of the tensile cracks (Figure 17(d)). The created cracks define four distinct parts of the wall, which rotate with respect to each other in an almost rigid manner, as sketched in Figure 17(e). Note that the diagonal cracking present in this test causes non-orthotropic damage states, which are difficult to model with closed-form models.

For the numerical simulation, the mesostructure of the material is made of bricks of dimensions $90 \times 30 \times 100 \text{ mm}^3$ with 10 mm thick mortar joints. The unit cell is discretized with a rather coarse mesh of 120 elements since the objective here is to illustrate the application of the scale transition. Two elements are used on the width of a joint. A biquadratic displacement field and a bilinear non-local strain field are used at the mesoscopic scale, together with plane stress assumption. Note that the compressive crushing observed in the last cracking stage of the experiment cannot be captured by this plane stress computation. A generalized plane state description would be useful in this respect, but would require a considerably finer mesoscopic discretization to simulate brick cracking [13]. A maximum principal stress criterion is used for the brick material and a Drucker–Prager criterion with a compressive cap is used for mortar. The same mesoscopic material parameters as reported in Table I are used, except for the intrinsic length scale, taken as $l_c = 2.2 \text{ mm}$, in order to keep a sufficient number of elements on the localizing zone with a coarser discretization. At the macroscopic scale a mesh of 48 elements is used with a biquadratic displacement interpolation and a four point integration scheme. Each iteration of the macroscopic solution procedure thus requires the solution of 192 mesostructural boundary value problems. A resultant compressive vertical load of 37.5 kN is considered for the first loading phase.

7.3.2. Numerical results. The load–displacement curve for the shear loading phase is shown in Figure 18. The computation was continued until loss of convergence, i.e. the post-peak response

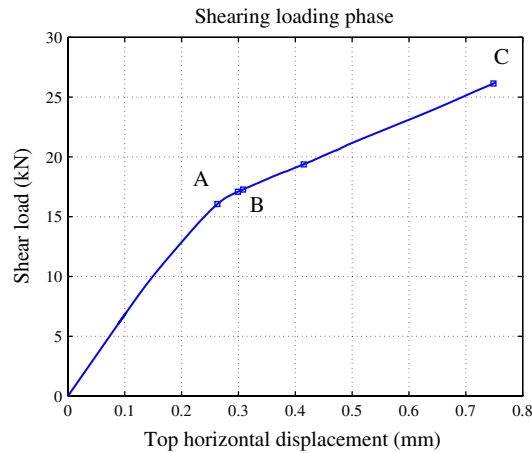


Figure 18. Load–displacement curve of shear loading phase.

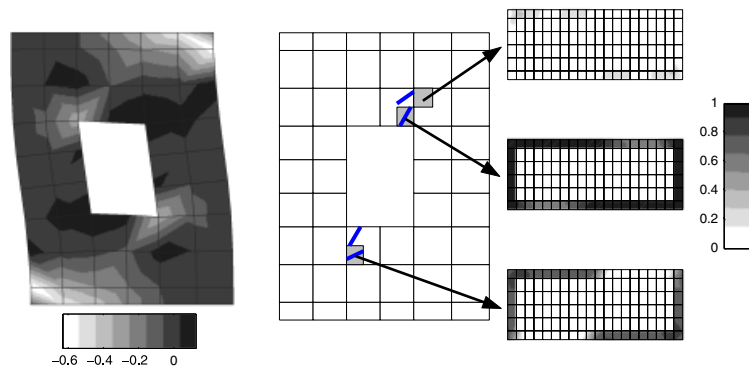


Figure 19. Damage state in stat A—initiation of diagonal cracking: macroscopic horizontal stress distribution (left), embedded discontinuities (centre), and mesoscopic damage states (right).

was not traced. The evolution of the macroscopic localization during the computation is illustrated in Figures 19–24 for each of the points A, B, and C in the load–displacement curve. In these figures, the embedded localization bands are represented with their respective orientations for the Gauss points in which localization has appeared. For each of these states the mesoscopic damage field in typical unit cells is shown. Unless stated otherwise, the unit cell damage patterns are related to the localization band of the Gauss point when a band is present. The macroscopic stress distribution is shown on the deformed shape of the structure—displacements have been magnified by a factor of 1000. As depicted in Figure 19, cracking initiates at the top right and bottom left corners of the opening. This crack initiation is due to horizontal tension combined with shear. At this stage, the orientation of the localization bands clearly reflects the staircase damage pattern obtained at the mesoscopic scale, which involves non-orthotropic damage effects. Some further damage evolution is already present in non-localized Gauss points, indicating that the diagonal

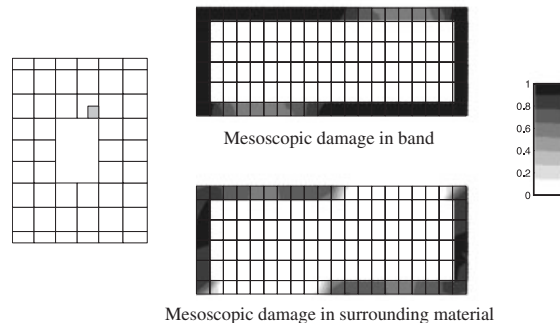


Figure 20. Damage state in state A with diagonal cracking: comparison between damage states inside and outside the localization band of the first localized Gauss point above the opening.

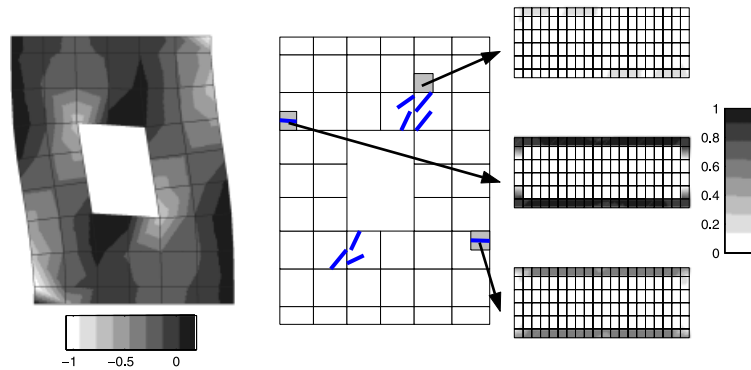


Figure 21. Damage state in state B—appearance of lateral horizontal cracks: macroscopic vertical stress distribution (left), embedded discontinuities (centre), and mesoscopic damage states (right).

cracking propagates in the direction of the corners of the wall. For the first localization band at the top of the opening, further damage evolution already influenced the staircase pattern in the situation represented in Figure 19. Fully anisotropic effects are however still present due to unloading of the material surrounding the localization band, which exhibits a staircase pattern as illustrated in Figure 20. The rather high level of damage reached in the surrounding material has a considerable impact on the aggregate response of this Gauss point, since the band occupies only a limited volume fraction of the associated material volume.

Upon further shearing, tensile damage zones localize at the edges of the wall as illustrated in Figure 21. During this stage, the existing diagonal cracks at the top and bottom of the opening do not evolve strongly (top unit cell in Figure 21). The multi-scale approach is thus able to represent the transition from the diagonal cracking to the tensile lateral cracking as observed in experiments on small structures of a similar shape (Figure 17). The comparison of the damaged state of the band and of the surrounding material for the tensile cracks is presented in Figure 22. A rather low damage level is obtained in the surrounding material as a result of the pure

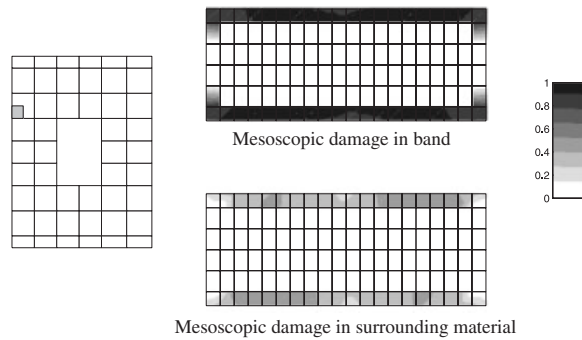


Figure 22. Damage state in state B with horizontal tensile cracking: damage states in the localization band and surrounding.

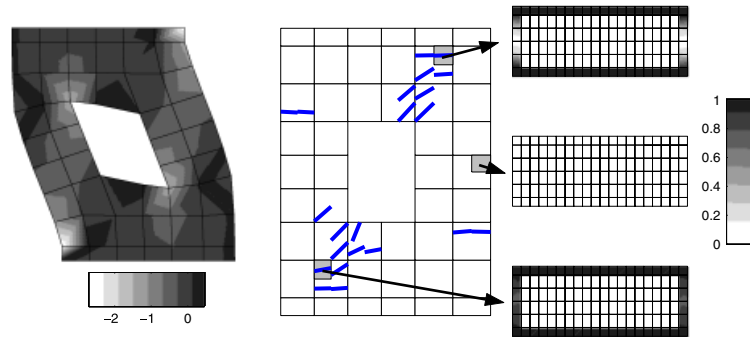


Figure 23. Damage state in state C—propagation of diagonal cracking: macroscopic vertical stress distribution (left), embedded discontinuities (centre), and mesoscopic damage states (right).

mode I opening of the bed joint, for which the behaviour becomes unstable early in the damaging process.

After the opening of the horizontal tensile cracks, the growth of the diagonal cracks near the opening is re-activated as observed in the experiments. This further propagation is accompanied by a reduced progression of the lateral tensile cracks. It is also observed that the embedded discontinuities near the corners of the wall tend to be inclined towards a horizontal direction, as shown in Figure 23 (top and bottom mesoscopic unit cells). The comparison between the damage state in the band and the surrounding material for a point located just below the top beam is illustrated in Figure 24. Even though damage is concentrated in the bed joints like for the horizontal tensile cracks (Figure 22), the level of damage in the surrounding is considerably higher here, which reflects that under the compressive stress path followed by this point, damage may grow substantially before triggering localization.

Finally, damage continues to grow in the direction of the corners of the wall, simultaneously with a reduced evolution of the lateral horizontal cracks (Figure 23). The result of this damage

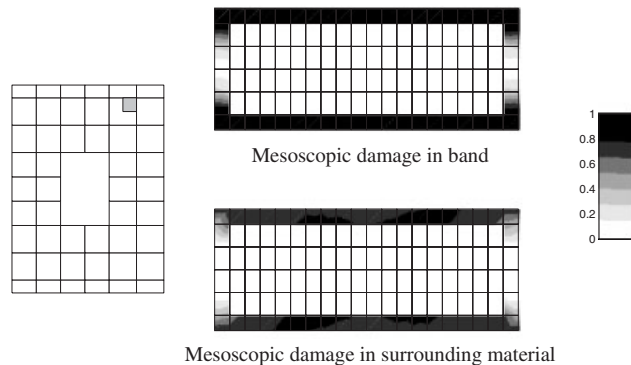


Figure 24. Damage state in state C with compressive bed joint damage: damage states in localization band and surrounding.

evolution is that strong redistributions of stresses occur, which lead to high compressive vertical stresses at four locations as observed in the experiments (Figure 23, left). Note also that the vertical tensile stress field is altered around the horizontal cracks by the presence of the damage, with a corresponding local decrease of this stress component. Figure 23 also confirms the presence of four highly compressed regions. The compressive failure at these locations represents the last stage of the cracking process as observed in experiments. The use of a generalized plane state would have an impact at this stage of the computation. Noteworthy is the fact that already at this stage, a good indication of the structural failure mechanism is found. The deformed shape of the wall depicted in Figure 23 shows that a mechanism is formed with the four parts of the cracked wall, which rotate with respect to each other.

It is emphasized that the last damage state represented in Figure 23 corresponds to a stage in which the final failure pattern is not reached yet since the post-peak branch of the structural response was not traced. Nevertheless, a qualitatively correct prediction of the evolution of damage is obtained by the multi-scale approach. In particular, the complex evolution of local cracking mechanisms (coupled to the appearance of mesoscopic damaging zones) is captured with the same sequence as observed experimentally.

8. CLOSURE

A localization-enhanced first-order multi-scale computational framework was proposed for the failure behaviour of masonry structures. The inherent complexity of this behaviour originates from the geometry of the material mesostructure which, for the case of masonry, is a well-known characteristic. The multi-scale scheme uses this well-defined geometry to avoid the formulation of complex macroscopic constitutive laws, by retrieving the overall response of the material from unit cell computations. The behaviour observed in these meso-analyses is transferred to the structural scale by a scale transition. Based on the homogenized tangent operator, it is possible to identify in a physically relevant way the onset and evolution of macroscopic localization. This is achieved using classical concepts of material bifurcation associated to the loss of ellipticity as

well as an eigenvalue analysis of the material tangent operator. In particular, it was shown that the detected localization orientation is aligned with the average orientation of the mesostructural damage patterns inside the unit cells for two typical loading schemes. As a result, a procedure for localization detection was defined and an enhanced first-order framework was sketched which allows the treatment of localization, by means of embedded bands introduced via a relaxed Taylor assumption. It is emphasized that the presented approach allows a mesostructurally motivated treatment of localization in masonry computations, both in terms of orientation and size of the localizing zone—a key feature for a proper representation of energy dissipation which is hardly found in existing models.

Because of the softening of the constituents, a snap-back may occur in the extracted homogenized material response, due to the averaging performed by the scale transition procedure. The scale transition and the path following method used in the macroscopic solution procedure have therefore been adapted to control this snap-back. This enhancement was achieved by steering the mesostructural scale computations onto a dissipative equilibrium path. Mesostructural equations related to the mesoscopic controlling degrees of freedom were transferred to the macroscopic solution procedure for this purpose. Computational details related to this coupled solution procedure were presented, including branch switching upon localization. Simple tests on homogeneously loaded macroscopic ‘structures’ were used in order to illustrate this approach. Finally, the application of the framework to structural computations was illustrated by means of a confined shear test on a wall with opening. It was shown that a qualitatively correct cracking evolution was obtained with this approach. Noteworthy is the fact that the principles of the presented framework are rather general and can be extended to other mesoscopic modelling strategies. In particular, the use of more detailed models based on mesoscopic interfaces for the representation of mortar joints is possible.

The proposed approach presents a complement to more efficient closed-form models for structural masonry computations. It allows the inclusion in structural computations of complex macroscopic material behaviour, related to the periodic mesoscopic geometry in connection with the presence of weak phases. The use of simpler constitutive models at the level of the constituents is possible in the proposed multi-scale approach, leading to an intrinsically accurate representation of the complex response at the structural scale (e.g. damage-induced anisotropy along preferential directions with non-orthotropic damage effects). Furthermore, the material identification of closed-form models is then transferred to the level of individual homogeneous phases, where it is believed to be more tractable. This higher flexibility obtained with the multi-scale approach is inherently accompanied by an increased computational cost compared to closed-form models. This aspect requires further work in order to avoid unnecessary mesoscopic computations in elastically behaving parts of structures, which could lead to a substantial decrease of the computational effort required.

ACKNOWLEDGEMENTS

The first author gratefully acknowledges the financial support from the Région Wallonne (Belgium) under grant 215089 (HOMERE).

REFERENCES

1. Lourenço PB. Experimental and numerical issues in the modelling of the mechanical behaviour of masonry. In *Structural Analysis of Historical Constructions II*, Roca P, Gonzalez JL, Oñate E, Lourenço PB (eds). CIMNE: Barcelona, 1998; 57–91.

2. Lourenço PB. Computations on historic masonry structures. *Progress in Structural Engineering and Materials* 2002; **4**:301–319.
3. Massart TJ, Peerlings RHJ, Geers MGD. Mesoscopic modelling of damage-induced anisotropy in brick masonry. *European Journal of Mechanics – A/Solids* 2004; **23**(5):719–735.
4. Lourenço PB, Rots JG. A multi-surface interface model for the analysis of masonry structures. *Journal of Engineering Mechanics* (ASCE) 1997; **123**(7):660–668.
5. Giambanco G, Rizzo S, Spallino R. Numerical analysis of masonry structures via interface models. *Computer Methods in Applied Mechanics and Engineering* 2001; **190**:6493–6511.
6. Lourenço PB, de Borst R, Rots JG. A plane stress softening plasticity model for orthotropic materials. *International Journal for Numerical Methods in Engineering* 1997; **40**(21):4033–4057.
7. Berto L, Saetta A, Scotta R, Vitaliani R. An orthotropic damage model for masonry structures. *International Journal for Numerical Methods in Engineering* 2002; **55**:127–157.
8. Papa E, Nappi A. Numerical modelling of masonry: a material model accounting for damage effects and plastic strains. *Applied Mathematics Modelling* 1997; **21**:319–335.
9. Halm D, Dragon A, Charles Y. A modular damage model for quasi-brittle solids—interaction between initial and induced anisotropy. *Archive of Applied Mechanics* 2002; **72**:498–510.
10. Anthoine A. Derivation of the in-plane elastic characteristics of masonry through homogenisation theory. *International Journal of Solids and Structures* 1995; **32**(2):137–163.
11. Cecchi A, Sab K. A multi-parameter homogenisation study for modelling elastic masonry. *European Journal of Mechanics – A/Solids* 2001; **21**:249–268.
12. Anthoine A. Homogenisation of periodic masonry: plane stress, generalized plane strain or three-dimensional modelling? *Communications in Numerical Methods in Engineering* 1997; **13**:319–326.
13. Pegon P, Anthoine A. Numerical strategies for solving continuum damage problems with softening: application to the homogenisation of masonry. *Computers and Structures* 1997; **64**(1–4):623–642.
14. Smit RJM. Toughness of heterogeneous polymeric systems. A modelling approach. *Ph.D. Thesis*, Eindhoven University of Technology, 1998.
15. Feyel F, Chaboche JL. FE² multiscale approach for modelling the elastoviscoplastic behaviour of long fiber SiC/Ti composite materials. *Computer Methods in Applied Mechanics and Engineering* 2000; **183**:309–330.
16. Kouznetsova V, Geers MGD, Brekelmans WAM. Multi-scale constitutive modelling of heterogeneous materials with a gradient-enhanced computational homogenisation scheme. *International Journal for Numerical Methods in Engineering* 2002; **54**:1235–1260.
17. Luciano R, Sacco E. Homogenisation technique and damage model for old masonry material. *International Journal of Solids and Structures* 1997; **34**(24):3191–3208.
18. van der Pluijm R. Out-of-plane bending of masonry—behaviour and strength. *Ph.D. Thesis*, Eindhoven University of Technology, 1999.
19. de Borst R, Sluys LJ, Muhlhaus HB, Pamin J. Fundamental issues in finite element analyses of localisation of deformation. *Engineering Computations* 1993; **10**:99–121.
20. Kouznetsova VG, Brekelmans WAM, Baaijens FTP. An approach to micro-macro modelling of heterogeneous materials. *Computational Mechanics* 2001; **27**:37–48.
21. Smit RJM, Brekelmans WAM, Meijer HEH. Prediction of the mechanical behaviour of nonlinear heterogeneous systems by multi-level finite element modelling. *Computer Methods in Applied Mechanics and Engineering* 1998; **155**:181–192.
22. van der Sluis O. Homogenisation of structured elastoviscoplastic solids. *Ph.D. Thesis*, Eindhoven University of Technology, 2001.
23. Massart TJ, Peerlings RHJ, Geers MGD, Gottcheiner S. Mesoscopic modelling of failure in brick masonry accounting for three-dimensional effects. *Engineering Fracture Mechanics* 2005; **72**:1238–1253.
24. Peerlings RHJ, de Borst R, Brekelmans WAM, de Vree JHP. Gradient-enhanced damage for quasi-brittle materials. *International Journal for Numerical Methods in Engineering* 1996; **39**:3391–3403.
25. Pijaudier-Cabot G. *Rupture et calculs à la ruine. These d'habilitation*, Université Paris VI Pierre et Marie Curie—LMT ENS Cachan, 1991 (in French).
26. Toupin RA. Elastic materials with couple stress. *Archives of Rational Mechanics and Analysis* 1962; **11**:385–414.
27. Mindlin RD. Micro-structure in linear elasticity. *Archives of Rational Mechanics and Analysis* 1964; **16**:51–78.
28. Rice JR. The localisation of plastic deformations. In *Theoretical and Applied Mechanics*, Koiter WT (ed.). North-Holland Publishing Company: Amsterdam, 1976.
29. Rice JR, Rudnicki JW. A note on some features of the theory of localisation of deformation. *International Journal of Solids and Structures* 1980; **16**:597–605.

30. Geers MGD. Enhanced solution control for physically and geometrically non-linear problems. Part I—The subplane control approach. *International Journal for Numerical Methods in Engineering* 1999; **46**:177–204.
31. Massart TJ. Multi-scale modeling of damage in masonry structures. *Ph.D. Thesis*, Eindhoven University of Technology & Université Libre de Bruxelles, 2003.
32. Sluys LJ, Berends AH. Discontinuous failure analysis for mode-I and mode-II localisation problems. *International Journal of Solids and Structures* 1998; **35**(31–32):4257–4274.
33. Jirásek M. Comparative study on finite elements with embedded discontinuities. *Computer Methods in Applied Mechanics and Engineering* 2000; **188**:307–330.
34. de Borst R, Wells GN, Sluys LJ. Some observations on embedded discontinuity models. *Engineering Computations* 2001; **18**(1–2):241–254.
35. Wells GN. Discontinuous modelling of strain localisation and failure. *Ph.D. Thesis*, Delft University of Technology, 2001.
36. Evers LP, Parks DM, Brekelmans WAM, Geers MGD. Crystal plasticity model with enhanced hardening by geometrically necessary dislocation accumulation. *Journal of Mechanics and Physics of Solids* 2002; **50**:2403–2424.
37. Massart TJ, Peerlings RHJ, Geers MGD. A dissipation-based control method for the multi-scale modelling of quasi-brittle materials. *Comptes-Rendus Mécanique* 2005; **333**(7):1–7.
38. Gutiérrez MA. Path-following constraint based on fracture energy control. In *Proceedings of the VII International Conference on Computational Plasticity—COMPLAS 2003*, Onate E, Owen DRJ (eds). CIMNE: Barcelona, 2003.
39. Kouznetsova VG. Computational homogenisation for the multi-scale analysis of multi-phase materials. *Ph.D. Thesis*, Eindhoven University of Technology, 2002.
40. Raijmakers TMJ, Vermeltoort ATH. Deformation controlled tests in masonry shear walls. *Technical Report B-92-1156*, TNO—Bouw, Delft, The Netherlands, 1992 (in Dutch).
41. Lourenço PB. Computational strategies for masonry structures. *Ph.D. Thesis*, Delft University of Technology, 1996.